The Eurasian Arctic Ocean along the MOSAiC drift (2019-2020): An interdisciplinary perspective on properties and processes

Kirstin Schulz[1,6,*], Zoe Koenig[2,3,4], Morven Muilwijk[3], Dorothea Bauch[5], Clara J. M. Hoppe[6], Elise S. Droste[6], Mario Hoppmann[6], Emelia J. Chamberlain[7], Georgi Laukert[8,9,10], Tim Stanton[11], Alejandra Quintanilla-Zurita[6], Ilker Fer[4], Céline Heuzé[12], Salar Karam[12], Sebastian Mieruch-Schnülle[6], Till Baumann[4,13], Myriel Vredenborg[6], Sandra Tippenhauer[6], Mats A. Granskog[3]

[1]Oden Institute for Computational Engineering and Sciences, The University of Texas at Austin, Austin, TX, United States

[2]UiT The Arctic University of Norway, Tromsø, Norway

[3]Norwegian Polar Institute, Fram Centre, Tromsø, Norway

[4]Geophysical Institute, University of Bergen and Bjerknes Centre for Climate Research, Bergen, Norway

[5]Leibniz-Laboratory, University of Kiel (CAU), Kiel, Germany

[6]Alfred Wegener Institute Helmholtz Centre for Polar and Marine Research, Bremerhaven, Germany

[7]Scripps Institution of Oceanography, University of California, San Diego, CA, United States

[8]GEOMAR Helmholtz Centre for Ocean Research, Kiel, Germany

[9]Department of Oceanography, Dalhousie University, Halifax, NS, Canada

[10]Woods Hole Oceanographic Institution, Woods Hole, MA, USA

[11]Oceanography Department, Naval Postgraduate School

[12]Department of Earth Sciences, University of Gothenburg, Gothenburg, Sweden

[13]Institute of Marine Research, Bergen, Norway

[*]corresponding author

This manuscript has been submitted for publication to Elementa: Science of the Anthropocene. If accepted, the final version of this manuscript will be available via the "Peer reviewed Publication DOI" link on the right-hand side of this page and will be available open-access on the publisher's website. For any question, contact the lead author Kirstin Schulz.

The Eurasian Arctic Ocean along the MOSAiC drift (2019-2020): An interdisciplinary perspective on properties and processes

Kirstin Schulz[1,6,*], Zoe Koenig[2,3,4], Morven Muilwijk[3], Dorothea Bauch[5], Clara J. M. Hoppe[6], Elise S. Droste[6], Mario Hoppmann[6], Emelia J. Chamberlain[7], Georgi Laukert[8,9,10], Tim Stanton[11], Alejandra Quintanilla-Zurita[6], Ilker Fer[4], Céline Heuzé[12], Salar Karam[12], Sebastian Mieruch-Schnülle[6], Till Baumann[4,13], Myriel Vredenborg[6], Sandra Tippenhauer[6], Mats A. Granskog[3]

[1]Oden Institute for Computational Engineering and Sciences, The University of Texas at Austin, Austin, TX, United States
[2]UiT The Arctic University of Norway, Tromsø, Norway
[3]Norwegian Polar Institute, Fram Centre, Tromsø, Norway
[4]Geophysical Institute, University of Bergen and Bjerknes Centre for Climate Research, Bergen, Norway
[5]Leibniz-Laboratory, University of Kiel (CAU), Kiel, Germany
[6]Alfred Wegener Institute Helmholtz Centre for Polar and Marine Research, Bremerhaven, Germany
[7]Scripps Institution of Oceanography, University of California, San Diego, CA, United States
[8]GEOMAR Helmholtz Centre for Ocean Research, Kiel, Germany
[9]Department of Oceanography, Dalhousie University, Halifax, NS, Canada
[10]Woods Hole Oceanographic Institution, Woods Hole, MA, USA
[11]Oceanography Department, Naval Postgraduate School
[12]Department of Earth Sciences, University of Gothenburg, Gothenburg, Sweden
[13]Institute of Marine Research, Bergen, Norway

[*]corresponding author

Abstract

The Multidisciplinary drifting Observatory for the Study of the Arctic Climate (MOSAiC, 2019/2020), a year-long drift with the Arctic sea ice, has provided the scientific community with an unprecedented, multidisciplinary dataset from the Eurasian Arctic Ocean, covering high atmosphere to deep ocean across all seasons. However, the heterogeneity of data and the superposition of spatial and temporal variability, intrinsic to a drift campaign, complicate the interpretation of observations. In this study, we compile a quality-controlled hydrographic dataset with best spatio-temporal coverage and derive core parameters, including the mixed layer depth, heat fluxes over key layers, and friction velocity. We provide a comprehensive and accessible overview of the ocean conditions encountered along the MOSAiC drift, discuss their interdisciplinary implications, and compare common ocean climatologies to these new data. Our results indicate that - for the most parts - ocean variability was dominated by regional, rather than seasonal signals, with potentially strong implications for ocean biogeochemistry, ecology, sea ice, and even atmospheric conditions. Near-surface ocean properties are strongly influenced by the relative position of sampling within or outside the river-water influenced Transpolar Drift, and seasonal warming and meltwater input. Ventilation down to the Atlantic Water layer in the Nansen Basin allows for a stronger connectivity to both sea ice and surface ocean, including elevated upward heat fluxes. The Yermak Plateau and Fram Strait region are characterized by variable conditions, strong ocean currents, a stronger influence of Atlantic Water, and substantial lateral gradients in surface water properties in frontal regions. Together with the presented results and core parameters, we offer context for interdisciplinary research, fostering an improved understanding of the complex, coupled Arctic System.

1. Introduction

To a large extent, the Arctic Ocean has been historically inaccessible due to its perennial ice cover, resulting in limited data availability, particularly during winter. With global warming triggering rapid transformations in the Arctic (Rantanen et al., 2022), a better understanding of processes in the Arctic Ocean and its role in the coupled climate system is urgently needed to accurately predict the effects of a changing climate. Ongoing changes in the Arctic Ocean include declining sea ice cover and longer open water seasons (e.g. Stroeve et al., 2008; Kwok, 2018; Kim et al., 2023), Atlantification, i.e., the progression of conditions typical for the North Atlantic further into the Arctic Ocean (Polyakov et al., 2017), a weakening upper ocean stratification, enhanced vertical mixing and transport (Polyakov et al., 2020b,a; Schulz et al., 2022a), increased primary productivity (Arrigo and van Dijken, 2015), and changes in the Arctic ecosystem composition (Gordó-Vilaseca et al., 2023). These changes are primarily observed in the Eastern Arctic, while conditions in the Western Arctic exhibit less clear patterns, e.g., no conclusive evidence of increased mixing (Dosser et al., 2021; Fine and Cole, 2022), or even show opposite trends, e.g., increased stratification by freshwater accumulation in the Beaufort Gyre (Timmermans and Toole, 2023).

The Multidisciplinary drifting Observatory for the Study of Arctic Climate (MOSAiC) was a recent (2019-2020), year-long drift campaign with the aim to improve our process-level understanding of the coupled Arctic System (Rabe et al., 2022; Shupe et al., 2022; Nicolaus et al., 2022). A large number of inter-disciplinary efforts in MOSAiC involve physical oceanography parameters, such as ocean temperature and salinity or current velocity. Examples include efforts to calculate the solubility of gases, to determine the origin of water masses that transport tracers and organisms, to quantify the contribution of oceanic heat to sea ice formation and melting, or to constrain the variability in ice-nucleating particles of marine origin. In addition, the modeling community requires updated oceanic boundary conditions and core parameters for model validation (Heuzé et al., 2023b), while climatological datasets, which are often crucial components in modeling frameworks, need ground-truthing to current conditions. However, the diversity of oceanographic equipment used during MOSAiC, and the resulting scattered datasets at various levels of processing and documentation hinder easy access to and utilization of these data, especially for non-physical oceanographers and scientists not involved in the field campaign. In addition, the design of MOSAiC as a drifting platform complicates the interpretation of oceanographic measurements. Superimposed on the annual cycle is the regionality along the more than 3500 km long drift track across the Eurasian basin (Rabe et al., 2022). These challenges might entail an inconsistent usage and interpretation of the oceanographical data, and hinder the inter-comparability of individual studies in the future.

In this study, we compile an accessible and quality-controlled dataset of hydrographic profiles at the highest possible temporal resolution along the drift, and provide derived core parameters (Schulz et al., 2023b), including an interactive data interface (Mieruch, 2023) in the online Ocean Data View webODV (Mieruch and Schlitzer, 2023), which can be consistently used in future disciplinary and interdisciplinary studies . Based on this dataset, we present a comprehensive overview of ocean conditions during the MOSAiC drift, discuss their effect on the coupled system, and - as far as possible - discriminate between spatial and temporal signals. This description of the state of the Eurasian Arctic Ocean in 2019-2020, and the comparison of commonly used climatological datasets to these modern data, will also aid the evaluation of ocean models.

The structure of this paper is as follows: In section 2, we provide a brief overview of the methods and instrumentation used in this study (more detailed information is available in the Appendix). Section 3 describes the geography along the drift track of MOSAiC, and in section 4 we summarize the water column structure and water mass distribution. Section 5 then focuses on dynamic features, such as surface and tidal current variability and eddies; and parameters related to ocean mixing, such as the vertical diffusivity and heat fluxes, are presented in section 6. In section 7, we compare MOSAiC results to existing climatologies. In the discussion (section 8), we contextualize the MOSAiC data by comparing them to previous findings, and we discuss the implications of these results for other scientific disciplines. Finally, section 9 summarizes the main findings and concludes the paper.

2. Methods and Instrumentation

The MOSAiC drift started in September 2019, using the icebreaker *RV Polarstern* (Knust, 2017) as a drifting platform frozen into the Arctic sea ice, with measurements conducted from the same ice floe and surrounding sites during five cruise legs. On-site sampling was interrupted between May 15 to June 27, 2020, due to the unavailability of a second icebreaker during the COVID-19 pandemic to perform personnel exchange and resupply, but resumed on the exact same floe. At the end of July, the floe disintegrated in the marginal ice zone in Fram Strait, and after relocation north, a second floe was chosen close to the previous drift track to sample the freeze-up period. In the following, we will briefly summarize the different datasets and methods used in this study. More details can be found in the Appendix, and an overview of the sampling locations is found in Rabe et al. (2022).

We obtain water depths from three different sources: The *Polarstern* echosounder, the combined altimeter and depth readings from the deep CTD (Conductivity, Temperature, Depth) casts, and the IBCAO v4.2 bathymetric dataset (Jakobsson et al., 2020). Drift track and speed are obtained from the *Polarstern* navigation records, and complemented with data from a GPS buoy ("CO1") that remained on the floe when sampling was interrupted in spring. From the drift velocity, we calculate the ice friction velocity $u_\star$ based on the Rossby similarity (see Appendix), as already done in Kawaguchi et al. (2022).

A set of in total 2,434 vertical temperature and salinity profiles are compiled, including data from the microstructure profiler (MSS) operated in Ocean City, i.e., a sampling site in the Central Observatory (CO) on the main floe (1,665 profiles, 0-350 m, Schulz et al. (2023c)), the Ocean City CTD (Tippenhauer et al. (in reviewa), 121 profiles, down to maximum 1000 m), and the *Polarstern* CTD (Tippenhauer et al. (in reviewb), 134 profiles, excluding those during transit). During the drift interruption, and on days without any MSS or CTD casts, we use profiles from the ice-tethered profilers ITP94 and ITP111 (down to 1000 m depth) (428 profiles in total, Toole and Krishfield, 2016), and daily mean data at five discrete depths (10, 25, 50, 75, 100 m) from a CTD chain on the Pacific Gyre buoy O4 (86 days, Hoppmann et al., 2022b), all deployed near the CO at the start of the drift. Data from all instruments are converted to Conservative Temperature Θ (°C) and Absolute Salinity S_A (g kg^{-1}), quality-controlled and cross-calibrated where necessary (see Appendix). Temperature readings from the *Polarstern* thermosalinograph are excluded here, as they were found to be unreliable (see Appendix), and we recommend these data are not used in future analysis.

We calculate the mixed layer depth, i.e., the vertical extent of the surface layer with uniform temperature, salinity, and hence density, as the first depth where the potential density anomaly σ_0 increases by more than $\Delta\sigma_0 > 0.04$ kg m^{-3} compared to the surface (4-10 m) mean value (or, 0.06 kg m^{-3} if the increase in density at the base of the mixed layer is more gradual, see Appendix). We omit giving mixed layer depth estimates in the presence of strong upper (0-10 m) ocean stratification (i.e., when there is no classical mixed layer, conditions frequently found during melt season), or when mixed layer depth estimates based on different density thresholds (0.04 to 0.08 kg m^{-3}) are very variable (i.e., the base of the mixed layer is not well defined). Surface salinity and temperature are calculated as the average over 4-10 m depth (to exclude sampling points within an under-ice meltwater lens in spring for the MSS), and the corresponding freezing point temperature is calculated based on the TEOS-10 set of equations (McDougall and Barker, 2011). Additionally, to better identify the surface water composition and origin, we calculate the surface layer (0-15 m) river water fraction based on an end-member analysis using δ^{18}O isotope and salinity measurements (Bauch et al., 2011), and CDOM (Colored Dissolved Organic Matter, an indicator for riverine water) fluorescence from ITP94 (legs 1-4 only) (e.g. Granskog et al., 2007; Gonçalves-Araujo et al., 2016; Stedmon et al., 2021). We characterize water masses and layers as summarized in Tab. 1.

Current velocity profiles ($\sim$20-400 m depth) obtained with a 75 kHz ADCP (Acoustic Doppler Current Profiler, Baumann et al., 2021) are used to calculate depth-averaged surface layer (14-30 m) and tidal (whole water depth) currents of different frequencies (see Meyer et al., 2017b, for more details in the methodology), and to visually identify eddies. Tidal velocities are compared to data from the tidal model AOTIM5 (Erofeeva and Egbert, 2020).

Table 1. Water mass and layer definitions. ML: Mixed Layer, HAL: halocline, THERM: thermocline, AAW: Arctic Atlantic Water, AW: Atlantic Water, UPDW: Upper Polar Deep Water, EBDW: Eurasian Basin Deep Water, EBBW: Eurasian Basin Bottom Water, CBDW: Canadian Basin Deep Water, AIW: Intermediate Water, NSDW: Nordic Sea Deep Water. σ_x is potential density referred at x km depth. Θ is Conservative Temperature.

Watermass	Upper limit	Lower limit	reference
ML	surface	base ML	this study (see Appendix)
HAL	base ML	$R = 0.05$	Bourgain and Gascard (2011)
THERM	$0.8\Theta_{\text{min, halocline}} < \Theta < 0.8\Theta_{\text{max, AW}}$		Schulz et al. (2021)
AAW	$0°\text{C} < \Theta < 2°\text{C}$		Korhonen et al. (2013)
AW	$\Theta > 2°\text{C}$		(Rudels et al., 2012)
UPDW	$\Theta = 0°$ C	$\sigma_{0.5} = 30.444$ kg m^{-3}	Rudels (2009)
EBDW	$\sigma_{0.5} = 30.444$ kg m^{-3}	$\sigma_1 = 37.46$ kg m^{-3}	Smethie Jr et al. (1988)
EBBW	$\sigma_1 = 37.46$ kg m^{-3}	sea floor	Smethie Jr et al. (1988)
CBDW	as EBDW/NSDW, but $\Theta > -0.6°$C, S_A >35.083[a]		Rudels (2009)
AIW[b]	$\Theta = 0°$ C	$\sigma_{0.5} = 30.444$ kg m^{-3}	Meyer et al. (2017b)
NSDW[b]	$\sigma_{0.5} = 30.444$ kg m^{-3} C	sea floor	Meyer et al. (2017b)

[a] Converted from Practical Salinity of 34.915 at 1500 m depth.
[b]Yermak Plateau and Fram Strait only.

Turbulent mixing parameters presented here are based on the dissipation rate of turbulent kinetic energy (ε), measured with the MSS (Schulz et al., 2022b). ε describes how much small (0.1-1 m) scale turbulent kinetic energy (”turbulence”) is present to mix the water column. From ε, we calculate the depth of the surface active mixing layer, i.e., the depth range where turbulence is elevated due to friction at the ocean-sea ice interface ($\varepsilon \geq 5 \times 10^{-9}$ W kg^{-1}). From ε and the local stratification, we calculate the turbulent diffusivity K_z along each profile, as described in Bouffard and Boegman (2013). This method takes into account how K_z scales in different energetic regimes, i.e., in the presence of high or low turbulence, and strong or weak stratification. Spatio-temporal averages in different regions or over certain vertical layers were obtained using the maximum likelihood estimator MLE (Baker and Gibson, 1987), and heat fluxes over the halocline and thermocline (see Tab. 1) were calculated following Schulz et al. (2021). In addition, eddy-correlation-based heat fluxes at 3 m depth were measured with an Autonomous Ocean Flux buoy at a distance of 15-25 km from *Polarstern* (see

Appendix for details).

We compare four typical Arctic Ocean climatological datasets, and two commonly used state estimates (i.e., models constrained with observational data to minimize the misfit to these observations), listed in Tab. 2 to the MOSAiC data. These data products cover different time periods, contain different types of data from various sources, and are produced using distinct methods and interpolation procedures (see Appendix for details).

Table 2. Climatologies and state estimates (*italic*) of temperature and salinity used for comparison with the MOSAiC observations (section 7).

Dataset	Reference	Temporal coverage
PHC3	Steele et al. (2001)	1948-1997
WOA18	Locarnini et al. (2018); Zweng et al. (2018)	1955-2017
MIMOC	Schmidtko et al. (2013)	1970-2011
WOA23	Boyer et al. (2018)	1991-2020
ASTE	Nguyen et al. (2021)	2002-2017
ECCOv4	Forget et al. (2015)	1992-2015

3. Geography along the drift track

The Arctic Ocean is a semi-enclosed basin, connected to the Atlantic Ocean via the Fram Strait between Svalbard and Greenland and the Barents Sea, and to the Pacific via the Bering Strait between Russia and Alaska. Surrounded by wide shelf seas, the deep Arctic basin is separated by the Lomonosov Ridge, which reaches from the Siberian to the Canadian shelf, into the Amerasian and Eurasian basins. The Eurasian Basin is further divided into the Amundsen Basin and the Nansen Basin by the Gakkel Ridge (Fig. 1a). The shallow Yermak Plateau extends from the continental shelf on which the Svalbard archipelago is located northwards, with the Nansen Basin on its eastern, and Fram Strait on its western side. These geographic divides have a large impact on Arctic Ocean circulation patterns, and hence on the water column structure in the different regions. When interpreting the results from a drift campaign such as MOSAiC, regional gradients have to be taken into account.

The MOSAiC drift started in October 2019 in the ~4400 m deep Amundsen Basin (green dot in Fig. 1), and progressed parallel to the Gakkel Ridge within the basin over virtually flat bottom topography for around five months. The drift then crossed the rough topography of the Gakkel Ridge over a three-week time period

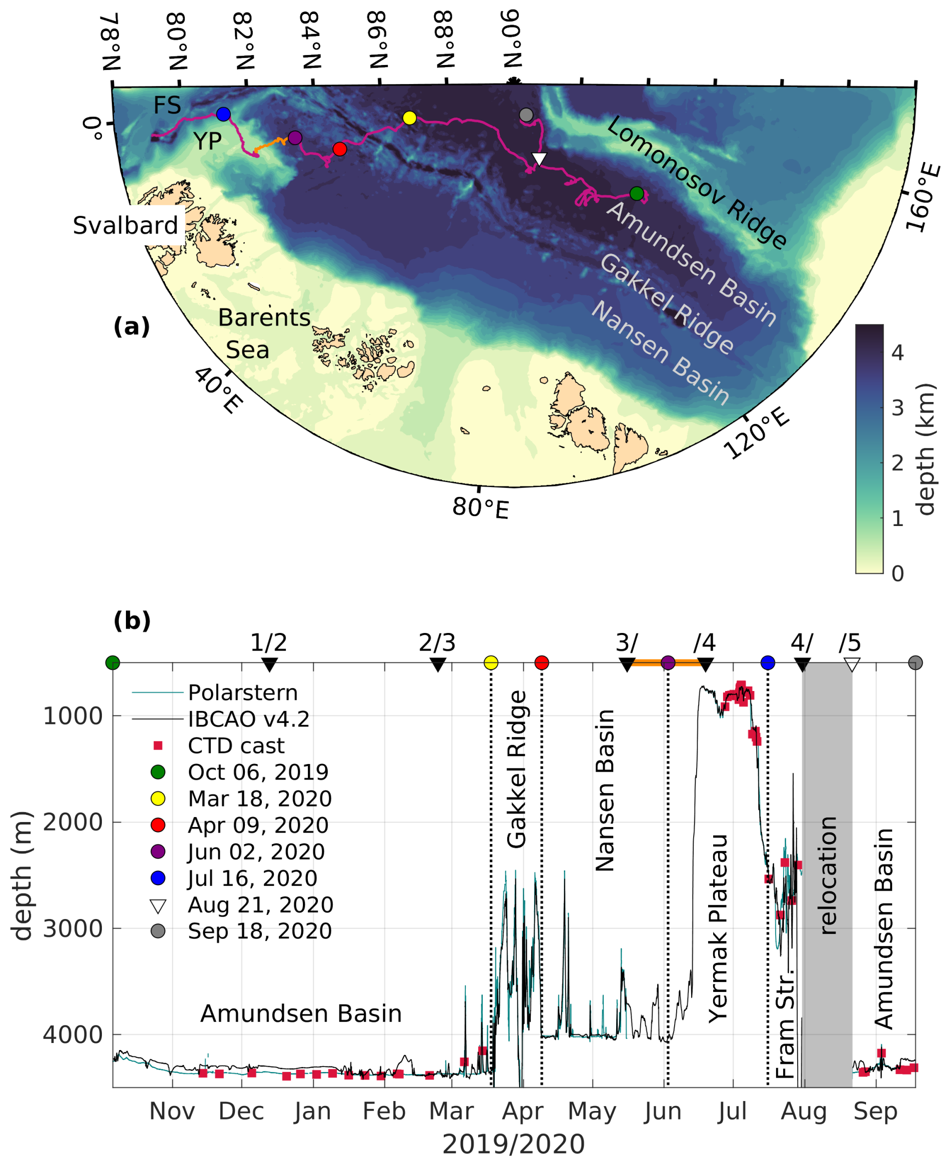

Figure 1. (a) Bathymetric map of the Arctic Ocean with drift track (violet from Polarstern, orange from GPS buoy CO1 between legs 3 and 4) indicated; (b) bathymetry along the drift track from Polarstern echosounder (teal), IBCAO v4.2 (black), and the deep CTD casts (red squares). For better orientation, landmarks of the drift, and the start and end of the individual legs, are indicated with colored dots and triangles in both figures. The orange line in (b) indicates the time period when the floe was left uncrewed.

between March 18 to April 9, 2020 (yellow to red dot in Fig. 1), and crossed the Nansen Basin. At the beginning of June, the drift reached the shallow Yermak Plateau (local depth ~800m, purple dot) northwest of Svalbard. After crossing the plateau from east to west, the floe entered the deeper waters and complex topography of Fram Strait on July 16 (blue dot in Fig. 1), and drifted south, until the floe eventually broke up in the marginal ice zone. After a relocation closer to the North Pole, in the vicinity of the previous drift track (white triangle in Fig. 1), measurements were resumed on a second floe in the Amundsen Basin. This time, the drift was directed northwards, parallel to the Lomonosov Ridge, until the expedition ended on September 20, 2020.

Compared to the water depth measurements from MOSAiC, we find that the bathymetric data from IBCAO v4.2 perform well in the basins and for the Gakkel Ridge and Yermak Platau region, but agree less well with the highly variable bottom depth in Fram Strait. In the following, we will use the bathymetric data from IBCAO, and any basin averages (e.g., of temperature and salinity profiles) will refer to averages over the regions indicated above and in Fig. 1b, with a discrimination between the Amundsen Basin winter (first part of the drift) and summer (last part of the drift) conditions.

4. Water column structure and variability

In the following sections, we provide a short general overview of the water masses of the Eurasian Arctic Ocean and their formation and characteristics (section 4.1). We will then elaborate on the observed variability of the near-surface waters (4.2), the Atlantic Water layer (4.3) and the deep water masses (4.4) during the MOSAiC drift.

4.1. Water masses in the Arctic Ocean

Large amounts of terrestrial freshwater (and other material) enter the Arctic Ocean from Siberia, and are advected towards Fram Strait together with sea ice formed on the Siberian shelves transported via the Transpolar Drift[1] (e.g. Rudels et al., 2012; Charette et al., 2020; Mysak, 2001; Karcher et al., 2012). These waters are characterized by high concentrations of dissolved organic carbon (DOC) and

[1]Both the transport of fresh water and sea ice across the Arctic Ocean are often referred to as the "Transpolar Drift". While both transport patterns are qualitatively similar, it should be kept in mind that the exact transport pathway and the velocity of sea ice and river water-rich surface water differ (see section 5). In this study, Transpolar Drift refers to the transport of relatively fresh, river water-rich surface water from Siberian regions towards Fram Strait, unless specified otherwise.

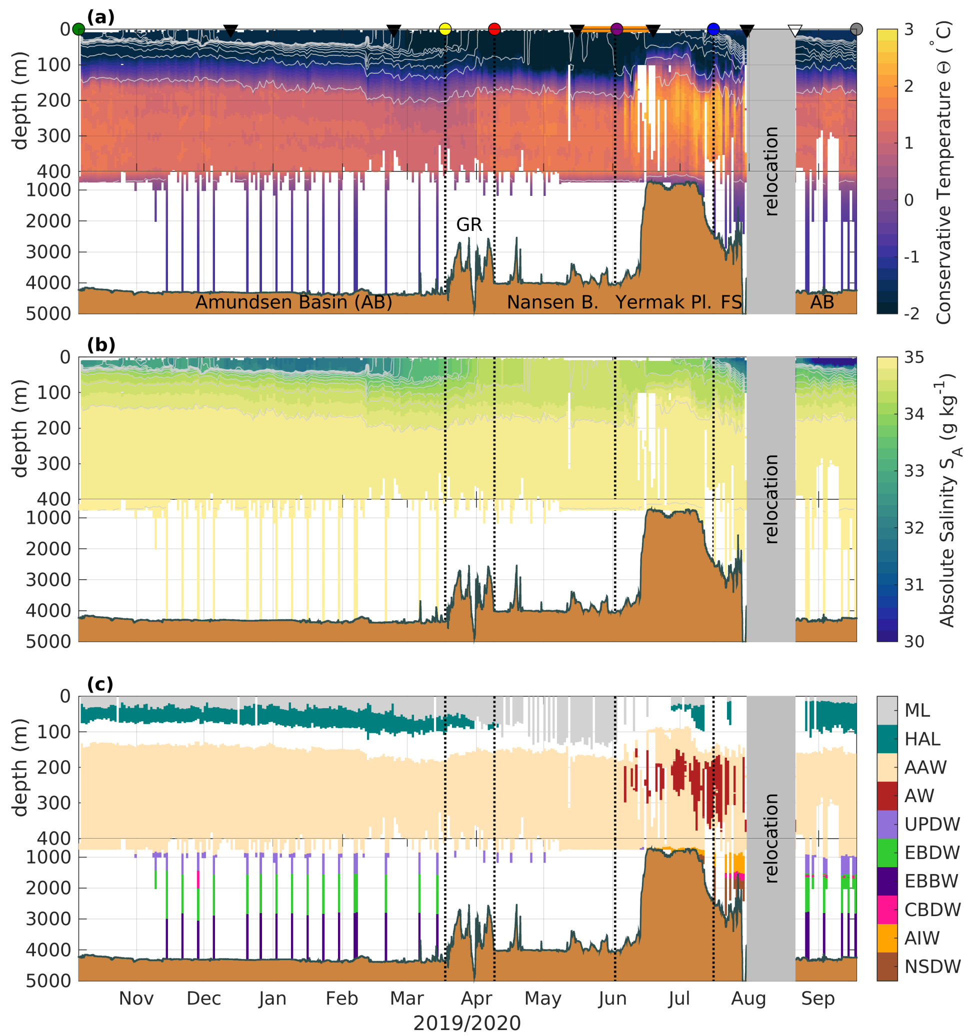

Figure 2. (a) Conservative Temperature (°C), (b) Absolute Salinity (g kg^{-1}), and (c) water mass distribution along the drift, based on the composite dataset presented in this study, with indicated topography (brown patches). Gray lines in (a) and (b) indicate isopycnals with a spacing of 0.2 kg m^{-3}. In (a) GR: Gakkel Ridge; in (c) ML: Mixed Layer, HAL: halocline, AAW: Arctic Atlantic Water, AW: Atlantic Water, UPDW: Upper Polar Deep Water, EBDW: Eurasian Basin Deep Water, EBBW: Eurasian Basin Bottom Water, CBDW: Canadian Basin Deep Water, AIW: Arctic Intermediate Water, NSDW: Nordic Sea Deep Water (see Tab. 1). Data gaps in June are caused by ITP profiles not covering the whole water column. Note that the y-axis is nonlinear, zoomed in the upper 400 m. In (a), triangles indicate the start and end of the legs, dots and vertical dotted lines the geographical markers, and the orange line the uncrewed period of the drift as in Fig. 1b.

various lithogenic elements, and may carry organisms originating from the coastal and shelf zones (Krumpen et al., 2019; Charette et al., 2020). Paffrath et al. (2021) showed, based on lithogenic provenance tracers, that most of the freshwater encountered in the Eurasian Arctic Ocean is derived from the Lena, Yenisei and Ob rivers, whose contributions do not fully mix and form distinct freshwater domains within the Transpolar Drift. The high nutrient load in these terrestrial waters is in parts consumed already on the wide Siberian shelves (Laukert et al., 2022, and references therein), and their role for primary production at the pan-Arctic scale is still not entirely clear (Fouest et al., 2013; Terhaar et al., 2021; Gibson et al., 2022). Mixed with ambient waters, this land-runoff forms a relatively fresh surface layer uniform in temperature and salinity: the polar mixed layer (ML, gray in Fig. 2c). This surface layer is bound by a pycnocline, i.e., a sharp increase in density, primarily set by salinity here, over a few meters, that we refer to as the base of the surface mixed layer. Below, salinity further increases, but more gradually, i.e., over tens of meters, with temperatures at or close to the freezing point. This layer is called the Arctic halocline (teal in Fig. 2c, Rudels et al. (2012); Schauer et al. (1997)). In temperature and salinity space (i.e., TS-diagrams), the halocline appears as an increase in salinity close to the freezing point line (Fig. 3a). Due to its strong stratification, the halocline suppresses the vertical exchange between the surface layer and underlying waters (Schulz et al., 2023a), and prevents both heat and nutrients from the Atlantic Water layer to reach the surface. In addition, the strong stratification also decouples the speed and even direction of lateral advection in the surface layer and halocline, which may all contribute to a heterogeneous distribution of tracers as well as microorganisms in these layers, despite being both located in the potentially sun-lit upper ocean.

Relatively warm and saline water from the Atlantic enters the Arctic Ocean through eastern Fram Strait and the shallow Barents Sea, carrying high nutrient concentrations (Torres-Valdés et al., 2013) and organisms of Atlantic origin (Snoeijs-Leijonmalm et al., 2022). This water circulates counterclockwise along the Arctic continental slopes (Schauer et al., 1997; Rudels et al., 2012), and is modified on its pathway by heat loss to the atmosphere when it resides close to the surface in the Barents Sea (Smedsrud et al., 2013; Meyer et al., 2017a), and subsequently by mixing with colder water masses (Lenn et al., 2009; Rippeth et al., 2015). This modification appears as a temperature decrease and a progressively deeper position of the warm and saline Atlantic Water within the water column along its advective pathway (e.g., Schulz et al., 2021). When Atlantic Water temperatures are below 2°C, we refer to it as modified, or Arctic Atlantic Water (AAW, see Tab. 1, beige in Fig. 2c). In TS-diagrams, this layer is visible as a temperature peak, i.e., an increase and decrease of temperature over a narrow salinity range (Fig. 3a). The distribution and modification of Atlantic Water can also be inferred from provenance tracers (e.g., Bauch et al., 2016; Laukert et al., 2017, 2019).

The identification of deep waters below the Atlantic Water layer is less straightforward, as changes in temperature and salinity at these depths can be close to the instrument precision (red box in Fig. 3). Moreover, historical definitions for these deep waters might not hold anymore, as the properties of the water masses involved in their formation have been changing due to ongoing global warming (Somavilla et al., 2013; von Appen et al., 2015). Here, we use a set of historical definitions that differ between the central basins and the regions of Yermak Plateau and Fram Strait (Tab. 1), but we advise treating these results with caution. In the central Eurasian Arctic Ocean (Amundsen and Nansen Basins), Upper Polar Deep Water (UPDW, lilac in Fig. 2c) resides below the Atlantic Water layer. UPDW is a heterogeneous water mass formed as a mixture of intermediate waters flowing into the Arctic Ocean through Fram Strait and Atlantic Water, which has been strongly cooled during winter in the Barents Sea, as well as saline and dense plumes formed on the shelves by brine rejection during sea ice formation (e.g. Rudels, 2009). In the TS-diagram, this water mass is a mostly straight line with increasing salinity and decreasing temperature (Fig.3b). Below the UPDW, the primary water mass is Eurasian Basin Deep Water (EBDW, green in Fig. 2c), with occasional intrusions of relatively warm and salty Canada Basin Deep Water (CBDW, pink in Fig. 2c). EBDW is characterized by nearly constant temperature and is the result of the interaction between inflowing deep waters through Fram Strait and dense plumes from the shelves (e.g. Smethie Jr et al., 1988). CBDW enters the Eurasian Basin across the Lomonosov Ridge and proceeds as a narrow boundary current, but is episodically transported into the interior basin by eddies. The water mass close to the sea floor is called Eurasian Basin Bottom Water (EBBW, dark purple in Fig. 2c), whose properties are impacted notably by dense overflows and geothermal heating (e.g. Smethie Jr et al., 1988). In Fram Strait, there is Arctic Intermediate Water (AIW, orange in Fig. 2c) instead of UPDW below the Atlantic Water layer, and Norwegian Sea Deep Water (NSDW, brown in Fig. 2c) closer to the sea floor. AIW is characterized by nearly constant salinity and decreasing temperatures with depth, and is typically enriched in oxygen, as it is formed through open ocean convection in the Nordic Seas (e.g. Meyer et al., 2017b). NSDW used to be seen as a cold, fresh and very dense water mass, but has warmed rapidly since the cessation of Nordic Seas deep convection, as it is no longer replenished. It now closely resembles EBDW (von Appen et al., 2015).

All the deep water masses are different mixtures between water of Atlantic origin and waters entrained by deep convection (NSDW) or dense water overflows (all Eurasian basins deep waters) and therefore have different tracer properties, especially oxygen (Karam et al., 2023) and transient tracers (Heuzé et al., 2023a).

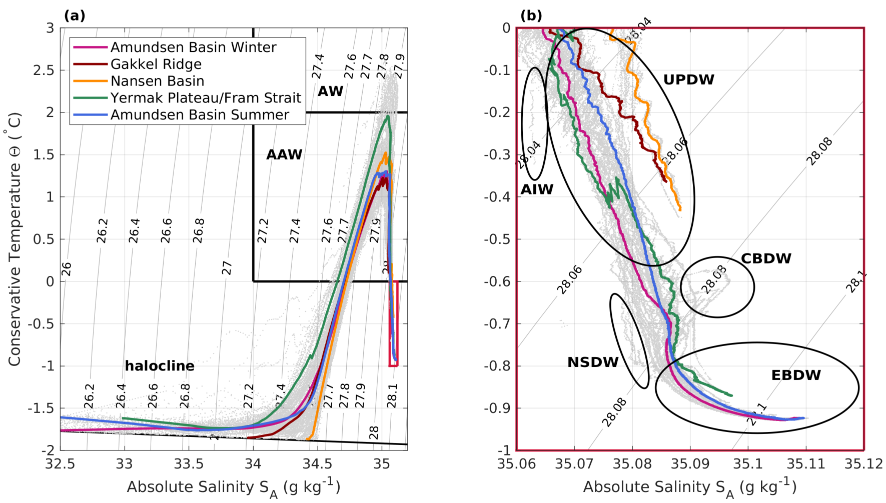

Figure 3. Temperature-Salinity diagram for (a) the full depth range (for the basin averages, the upper 5m are not shown); and (b) enlargement of the deep water masses. Gray lines indicate daily profiles, colored lines refer to basin averages as indicated. The black line in (a) indicates the salinity-dependent freezing point temperature, black rectangles indicate Atlantic Water (AW) and Arctic Atlantic Water (AAW). The small red rectangle in (a) corresponds to the range displayed in (b).

4.2. Surface and Subsurface Layer Properties along the MOSAiC Drift

The Amundsen Basin in early winter is characterized by a well-defined surface mixed layer near freezing point of around 30 m depth, and a stable halocline below (Fig. 4a,d). Intermediate surface salinities around 33 g kg^{-1} combined with low CDOM concentrations (Fig. 4b,c) suggest that the contribution of river water is relatively small here. However, neodymium and oxygen isotopes (data not shown), which can be used as provenance tracers, indicate distinct river water contributions from Yenisei and Ob, suggesting partial surface water advection from the Kara Sea

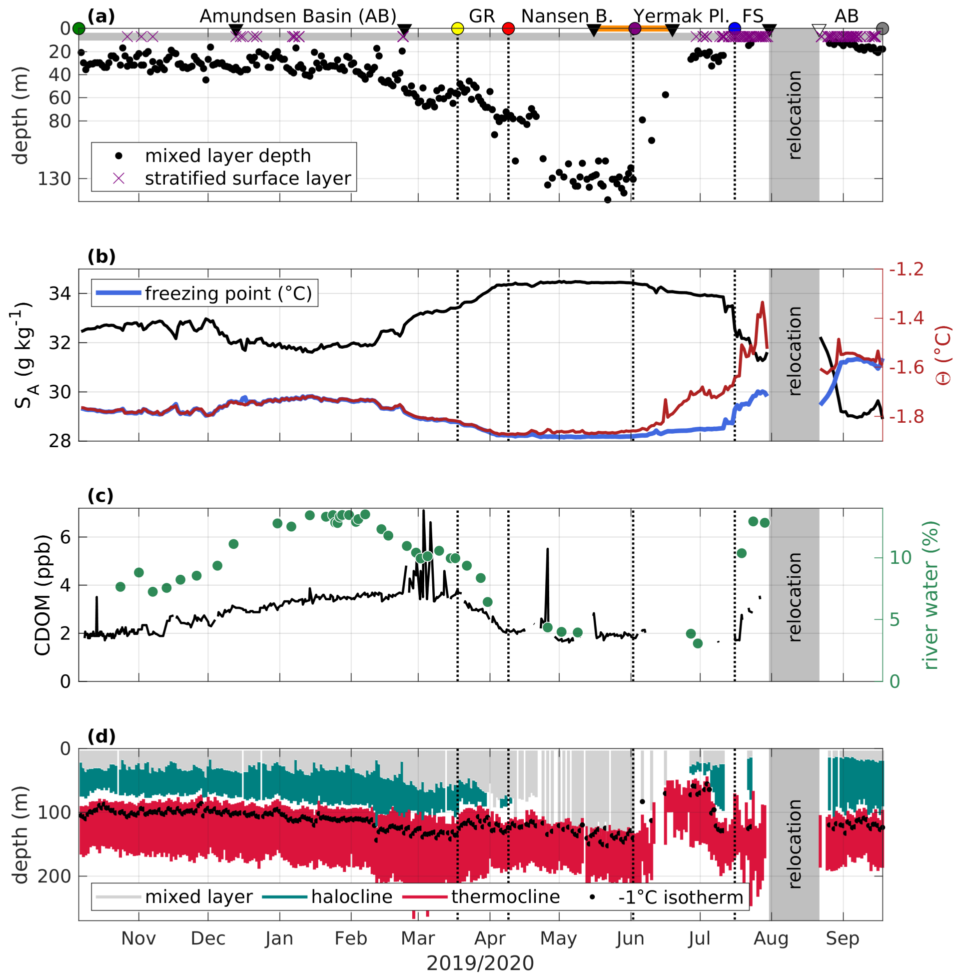

Figure 4. Surface (mixed) layer (a) depth (m, black dots, stratified surface layers are indicated with purple crosses); (b) Absolute Salinity (g kg^{-1}, black line), Conservative Temperature Θ (°C, red line) and freezing point temperature (°C, blue line); (c) colored dissolved organic matter (CDOM, ppb, black line) and river water fraction (%, green dots); and (d) mixed layer (gray), halocline (teal) and thermocline (red) extent, and position of the -1 °C isotherm (black dots) along the drift. In (a), triangles indicate the start and end of the legs, dots and vertical dotted lines the geographical markers, and the orange line the uncrewed period of the drift as in Fig. 1b.

(Laukert et al., in prep). Sea ice meltwater from the preceding melt season may also contribute to a fresher surface layer in this region (compared to the water below) and dilute the river-borne compounds. This could explain the rather low dissolved organic carbon (DOC) concentrations at the very start of the drift (Kong, 2022). At the beginning of December, a decrease in salinity and an increase in both CDOM and river water fraction (derived from δ^{18}O, see section 2, Appendix) to over 13 % indicate that the floe enters the river water-rich part of the Transpolar Drift. Somewhat surprisingly, the position of the maximum river water fraction does not coincide with the highest concentrations of CDOM, which appear only when surface salinity increases again, and the surface layer starts to deepen in March (Fig.4a,b,c). This could be related to different freshwater sources and their respective advective pathways, as the distribution of neodymium isotopes indicates alternating freshwater domains in this region either reflecting increased contributions from the Yenisei and Ob rivers or the Lena River (Laukert et al., in prep). A similar but spatially shifted distribution has already been described based on summer data from 2015, suggesting a strong spatio-temporal variability of the surface waters in the Eurasian Arctic Ocean (Paffrath et al., 2021).

When approaching Gakkel Ridge, the floe leaves the heavily river-water influenced part of the Transpolar Drift, and surface salinity increases to a maximum of 34.3 g kg^{-1}. River water fraction and CDOM concentrations decrease during the passage of the ridge (Fig.4c). This is also coincident with a decrease of DOC concentrations in the surface layer (Kong, 2022). On the Nansen Basin-side of the Gakkel Ridge, the surface mixed layer deepens to around 80 m, and at the end of April, the surface stratification, i.e. the halocline, disappears completely, and density only increases at a depth of $\sim$130m. These conditions have previously been described as "deep ventilation" (Polyakov et al., 2017), referring to a mixed layer that is not bounded by the halocline but reaches down to the warm Atlantic Water layer. This enhanced connectivity between the surface and Atlantic layer, compared to the situation in the Amundsen Basin, is also evident from provenance tracer distributions suggesting enhanced Atlantic Water admixture to the surface (Laukert et al., in prep), and might promote the transport of deep oceanic heat towards the sea ice (see section 6), thereby slowing basal growth (Lei et al., 2022), and increase vertical nutrient supply to the surface layer (Randelhoff et al., 2020). The enhanced vertical exchange might also facilitate the transport of organisms advected in the Atlantic Water layer closer to the surface. Deep ventilation, along with relatively constant surface salinity, low river water fraction and CDOM concentrations, persists throughout the Nansen Basin, until the drift reaches the Yermak Plateau in June (Fig.4).

Above Yermak Plateau, from the end of May onwards, surface layer temperatures increase successively with ongoing solar warming and deviate more and more from the freezing point (Fig. 4b). River water fraction and CDOM remain at the same low levels as encountered in the Nansen Basin, but a slightly lower surface salinity allows for the presence of a halocline. The Atlantic Water layer on the eastern side and above the plateau is much shallower (see section 4.3), restricting the vertical extent of the halocline (Fig. 4d). Sea ice melt, starting in late May to early June (Webster et al., 2022; Lei et al., 2022), and surface warming create vertical density differences, i.e., stratification, within the near-surface layer. Turbulent mixing in the upper ocean (see section 6 for details) does not penetrate deeper than 30 m, and is usually not strong enough to destroy the near-surface stratification established by meltwater input and warming. Hence, especially later in the season, we often observe no classical surface mixed layer (purple crosses in Fig. 4a), and even in the uppermost layer, vertical gradients in any tracer concentration, e.g., nutrients, or organism distribution, can be expected.

When leaving Yermak Plateau, on July 16, we observe another regime shift in the surface layer: Surface salinity abruptly decreases, while river water fraction and CDOM concentrations, which had remained low since entering the Nansen Basin, increase. This change is accompanied by a trend toward less radiogenic neodymium isotopic compositions (Laukert et al., in prep), suggesting increased admixture of Lena River water and supporting cross-Arctic transport of Siberian freshwater. In Fram Strait, we also observe a subsurface increase of CDOM (data not shown), indicative of the ”edge” of the East Greenland Current (which is an extension of the Transpolar Drift of relatively fresh water of Siberian origin). Such a transition from one oceanic (surface) regime to another is often accompanied by sudden changes in biogeochemical water properties (e.g., nutrient relationships) and potentially also the ecological community structure (e.g., Tippenhauer et al., 2021). Surface temperature anomaly relative to freezing point further increases, to maximum 0.4°C shortly before the floe broke up.

After relocation north at the end of August, back into the Amundsen Basin, we observe the freshest surface waters (see also Rabe et al., 2022), and a stable halocline similar to the first phase of the drift. There are no sensor-based CDOM measurements after the relocation, but the highest CDOM absorption and DOC concentrations in surface waters during MOSAiC were found here (Kong, 2022). Moreover, the highest river water fractions based on oxygen isotopes and the least radiogenic neodymium isotope signatures were determined, in line with the strongest Lena River contributions during the entire MOSAiC campaign (Laukert et al., in prep). The similarity of neodymium isotope signatures between this freshwater domain and that in the western Fram Strait may suggest continuous freshwater transport along the Transpolar Drift. However, there are other sources of freshwater in the western Fram Strait, e.g., water originating from the Beaufort Gyre, and enhanced freshwater export from the Siberian shelf exhibits a strong seasonality linked to the variable shelf hydrography (Janout et al., 2020). The uppermost layer is often stratified due to sea ice melt and solar warming. Whenever a well-defined surface layer exists, it is about 20 m deep, slightly shallower than during the first part of the drift. Surface temperatures were still above freezing when sampling resumed, but approached freezing point at the beginning of September.

In addition, when resuming sampling on leg 4 in July, we observe an approximately 1 m thick, low-salinity (S_A from close to 0 to about 10 g kg^{-1}) under-ice meltwater layer, also manifested with the presence of false bottoms (Smith et al., 2022; Salganik et al., 2023a), and visible in salinity profiles (Schulz et al., 2022b). During both legs 4 and 5, low salinity meltwater layers in leads remains present until strong winds caused enhanced mixing between September 5–9 (Smith et al., 2023; Nomura et al., 2023). The presence of meltwater results in a very strong stratification in the uppermost meters, up to two orders of magnitude stronger compared to the halocline. Measurements with an uprising turbulence profiler also show drastically reduced turbulent mixing in the near-surface layer when meltwater layers were present Fer et al. (2022). Details on the dynamics and implications of meltwater layers can be found in Smith et al. (2023, 2022); Salganik et al. (2023a); Nomura et al. (2023).

4.3. Atlantic Water Layer along the MOSAiC Drift

Modified Arctic Atlantic Water (AAW) is present throughout the MOSAiC drift. In the Amundsen Basin, the upper limit of the AAW layer is situated at $\sim$150 m depth. After passing the Gakkel Ridge into the Nansen Basin, the AAW is warmer and situated deeper in the water column (Fig.2a). Relatively unmodified Atlantic Water (AW), coming straight from the Atlantic and being characterized by a core temperature above 2°C, is only present above Yermak Plateau (Fig. 2c), where warm waters also reside about 100 m closer to the surface (Fig. 4d), and in Fram Strait. In this manuscript, we use the term Atlantic Water (layer) to refer to both AW and AAW.

The ”older” the Atlantic Water layer, i.e., the longer it has not been in contact with the surface and traveled in the Arctic while being mixed with colder waters, the deeper and colder its core (Rudels, 2015). Hence, we observe a strong correlation ($R^2 = 0.67$, not shown) between the core depth and the core temperature. Along the drift in 2019-2020, the Atlantic Water core was mostly located at around 300 m depth, with a temperature around 1.2°C. Above Yermak Plateau and in Fram Strait, the core is approximately 1°C warmer (and 0.1 kg m^{-3} lighter) and 100 m shallower, but subject to strong variability. In this region, the impact of the shallow and ”young” Atlantic Water on e.g., nutrient supply or organism composition, might be more pronounced compared to the situation in the deep basins.

As Atlantic Water can take different paths within the Arctic Ocean, e.g., entering via Fram Strait or through the Barents Sea, or recirculating into the deep basins from different positions along the continental slope (Rudels et al., 2012; Rudels, 2015), different branches of Atlantic Water, with slightly different temperature and salinity signatures, can often be found at the same position, stacked on top of each other (Rudels and Hainbucher, 2020). These ”interleaving” layers can be identified as z-shapes near the Atlantic Water temperature maximum in the TS-diagrams (Figure 3a), and as inversion layers and local temperature minima in the temperature profiles. In the Amundsen and Nansen Basin, interleaving involves mainly the Barents Sea and the Fram Strait branches of Atlantic Water. In the more dynamic Fram Strait region, we find strong interleaving, with several sources of Atlantic Water, which might differ in their respective biogeochemical signature that cause vertical gradients in, e.g., nutrient concentration.

In addition, at the upper bound of the Atlantic Water layer, both temperature and salinity increase with depth. In quiescent conditions, i.e., when turbulent mixing is negligible, and molecular diffusion is the dominant mixing process, temperature gradients diffuse faster than gradients in salinity. This difference in thermal and haline diffusion coefficients creates step-like structures, so-called thermohaline or double-diffusive staircases, typical for the Arctic Ocean (Shibley et al., 2017). These structures can persist for years and over 100 km of horizontal distance, and individual layers can be up to several 10 m thick (e.g. Lenn et al., 2009; Guthrie et al., 2017). Along the MOSAiC drift, we frequently, but not always, observe thermohaline staircases in the quiescent Amundsen Basin, in line with findings from high resolution observations from drifting stations in the same area, that show 1-3 m thick thermohaline staircase layers in the 200–260 m depth range (Sirevaag and Fer, 2012). Outside of the Amundsen Basin, we sometimes see structures that might be remnants of thermohaline staircases in the vertical profiles (not shown), but their characteristic sharp interfaces are absent. These differences point towards a lower connectivity between surface and deeper ocean in the Amundsen Basin, compared to the other parts of the drift.

4.4. Deep Water along the MOSAiC Drift

The deep water masses during the MOSAiC drift are already described in detail in Karam et al. (2023) and Rabe et al. (2022), and we only provide a brief summary here. Despite the uncertainties associated with the identification of deep water masses (sensor accuracy, changes in end member properties, see section 4.1), we observe a somewhat consistent distribution of deep waters across the Eurasian basin during MOSAiC. In the Nansen and Amundsen Basin, we see UPDW right under the Atlantic layer down to $\sim$1500 m. Below the UPDW, we primarily find EBDW until the sill depth of Fram Strait ($\sim$2500 m) and we occasionally see intrusions of relatively warm and salty CBDW as a salinity maximum between 1700-2000 m depth (Karam et al., 2023). Below the sill depth of Fram Strait, the temperature increases slightly as we encounter the last deep water mass, EBBW, until the sea floor. Further efforts are ongoing to, e.g., determine the contribution of these deep waters to anthropogenic carbon storage. Deep waters directly above Gakkel Ridge and their unique hydrothermal-vent-influenced ecosystem were not sampled during MOSAiC.

The deeper waters above Yermak Plateau and in Fram Strait consist of UPDW, alternating with likely AIW. Below UPDW/AIW, we can again observe CBDW in Fram Strait, as a salinity maximum at roughly 2000 m depth. Close to the bottom in Fram Strait, we find a mixture of NSDW and EBDW. Again, we note that identifying water masses in Fram Strait solely based on their temperature and salinity signature as done in this study is associated with large uncertainties, primarily due to the warming and increased salinity of waters south of Fram Strait over the past decades. Hence, traditional water mass classifications (Marnela et al., 2016) do not necessarily hold for the deep waters anymore (Somavilla et al., 2013; von Appen et al., 2015). Other tracers, such as CFC, SF_6, or dissolved oxygen, are needed to accurately determine the origin of deep water masses, which is beyond our scope and addressed in Karam et al. (2023) and Heuzé et al. (2023a).

5. Current Velocities, Tides, and Eddies

In both central basins, current velocities below the surface mixed layer are small, on the order of 0.01 m s^{-1}. Within the surface mixed layer, current velocities are intensified and correlate with the sea ice drift speed (R^2=0.9, data not shown). The magnitude of the ocean surface current (14-30 m vertical average), however, is much smaller, on average 16 % of the floe drift speed (Fig. 5a), meaning the ice moves around six times faster than the upper ocean. This difference illustrates that, while both sea ice and fresh, riverine water are transported from their region of

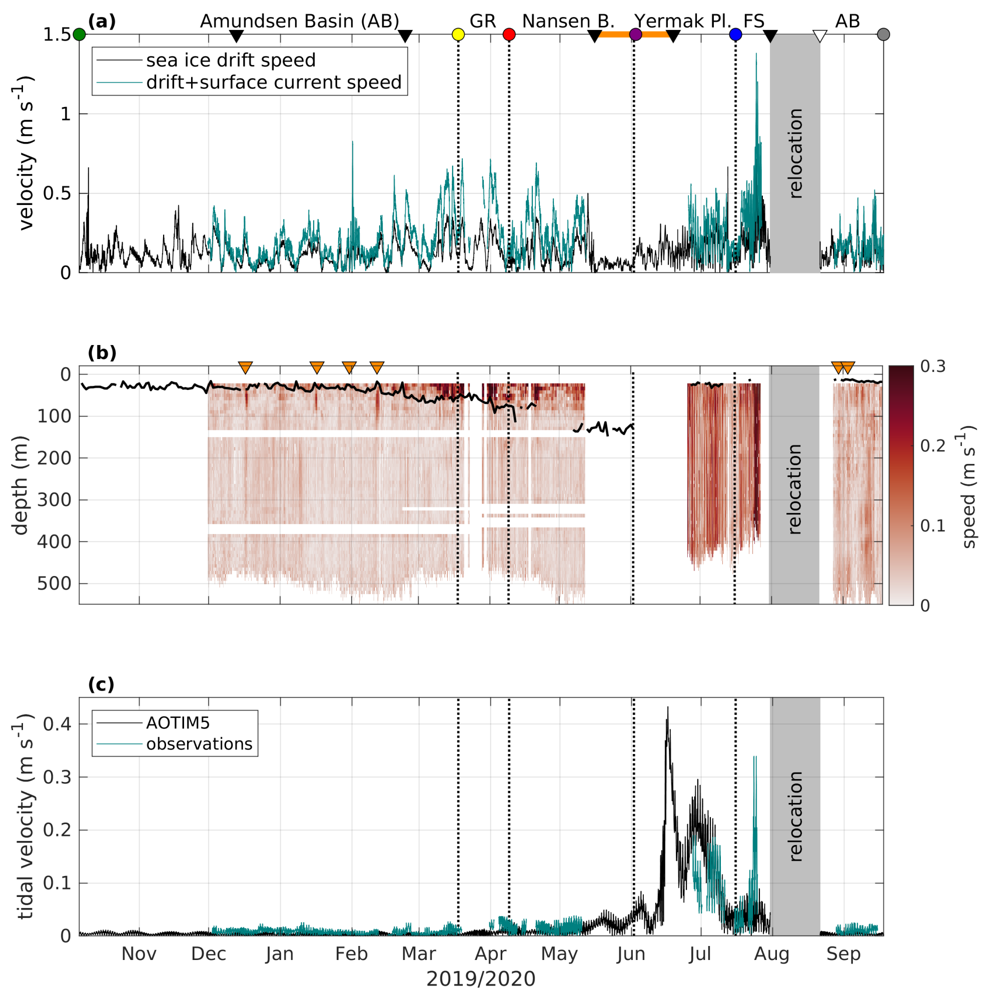

Figure 5. **(a) Sea ice drift (black, m s^{-1}) and combined drift and averaged current velocity in the upper 14-30 m relative to the floe (teal, m s^{-1}), (b) current speed (m s^{-1}) relative to the sea floor; and (c) tidal velocities (m s^{-1}) from observations (teal) and the AOTIM5 inverse tidal model (black) along the drift. In (a), triangles indicate the start and end of the legs, dots and vertical dotted lines the geographical markers, and the orange line the uncrewed period of the drift as in Fig. 1b. In (b), orange triangles indicate the time of the major eddies, the black line indicates the depth of the surface mixed layer.**

origin in Siberia across the Arctic towards Fram Strait, their transport timescales and exact pathways differ. Sea ice within the Transpolar Drift typically traverses the Arctic Ocean within 1-3 years (Charette et al., 2020; Steele et al., 2004), while the transport timescale for fresh water might be rather on the order of a decade. In addition, the pathway of the Transpolar Drift is strongly influenced by daily to decadal variability in wind conditions (Mysak, 2001), yielding that liquid and solid fresh water of similar origin in space and time might take very different routes through the Arctic Ocean. The difference in sea ice drift and surface ocean current speed also underlines that, while sampling the same sea ice, the water below the ice quickly changes throughout the drift, and oceanic data cannot be treated as a simple time series. Furthermore, as the surface mixed layer tends to move faster than the ocean below, any time series recorded above and below the surface mixed layer base might develop independently of each other.

The region around Yermak Plateau, and especially in Fram Strait, is more energetic. Absolute current velocities are much higher (up to 0.4 m s^{-1}), more variable, and surface currents correlate less with sea ice drift. Here, tides play a greater role, with a dominance of diurnal frequencies above Yermak Plateau, and semi-diurnal frequencies in Fram Strait (data not shown, see Fer et al., 2015, for details on tides in the region). In combination with the more variable water column structure in this region (see section 4), we expect more variability on short, daily to sub-daily, timescales, e.g., in surface nutrient supply or species composition. Assumptions of lateral homogeneity, i.e., negligible spatial gradients, which are to some degree justified in the respective deep basins, do not hold anymore in the dynamic regime of Yermak Plateau and Fram Strait.

Table 3. Main eddies observed during the MOSAiC drift. D is the first depth where the eddy is detected, $\triangle$h is the vertical eddy thickness.

Start (UTC)	End	D (m)	$\triangle$h (m)	Type
17.12.19 01:00	18.12.19 11:00	38	40	Anticyclonic
16.01.20 07:00	17.01.20 10:00	38	48	Anticyclonic
31.01.20 08:00	02.02.20 07:00	22	56	Anticyclonic
11.02.20 14:00	13.02.20 12:00	22	80	Anticyclonic
29.08.20 17:00	30.08.20 17:00	38	40	Cyclonic
03.09.20 23:00	03.09.20 10:00	30	64	Anticyclonic

Six main eddies were identified in the halocline in the Amundsen and Nansen Basin, listed in Tab. 3 and indicated in Fig. 5b. Five of these eddies rotated anticyclonically (clockwise), and only one cyclonically. The timing of these eddies does not coincide with the presence of storms or strong winds, indicating the eddies have not been formed locally, but might rather be advected and originate from topographic features (Zhao et al., 2014). Eddies can transport water masses with distinct biogeochemical signatures over large distances, and their associated higher current velocities can increase local vertical mixing (Son et al., 2022). Both processes can enhance the nutrient supply to the photic zone, making eddies potential biological hotspots. Any nutrients supplied by eddy activity in the Arctic winter would not be consumed, but (locally) increase the nutrient inventory for the next productive season. In addition, anticyclonic eddies are associated with a shoaling of the mixed layer base, most pronounced for the eddies in January and February, where the mixed layer depth decreased by 10-20 m. However, a similar variability in mixed layer depth is also observed during times when eddies were absent. In the Yermak Plateau/Fram Strait region, eddy activity is obscured by the strong tides; hence no eddies were identified there.

On November 9, 14, and 28 (2019), we also observed a large anticyclonic eddy at greater depth, indicated by sloping isopycnals above and below the eddy, with relatively dense waters above the eddy and light waters below, relative to the adjacent water column (data not shown). The eddy carries a warm and salty CBDW intrusion, and extends over approximately 1200-2400 m depth (Karam et al., 2023).

6. Turbulence and Vertical transport

6.1. Surface Mixing

In contrast to the surface *mixed* layer depth, which describes the depth to which the surface layer is uniform in temperature and salinity (see section 4.2), the *mixing* layer depth describes how deep active turbulent mixing - which is created by friction at the ice-ocean interface, or by wind and waves in the marginal ice zone or open water conditions - penetrates into the water column. While active mixing creates the mixed layer by homogenizing the water column, the mixed layer will persist even after the active mixing has decayed. That is because the small-scale turbulent motion causing the mixing will dissipate within hours or days, but the re-establishment of gradients near the surface, i.e. re-stratification, often takes much longer, especially in the absence of restoring forces, such as strong lateral gradients. This is the reason why the distribution of biological and biogeochemical tracers is often homogenous in the actively mixing layer, but not in the mixed layer, where it instead reflects a combined signal of past active mixing and new

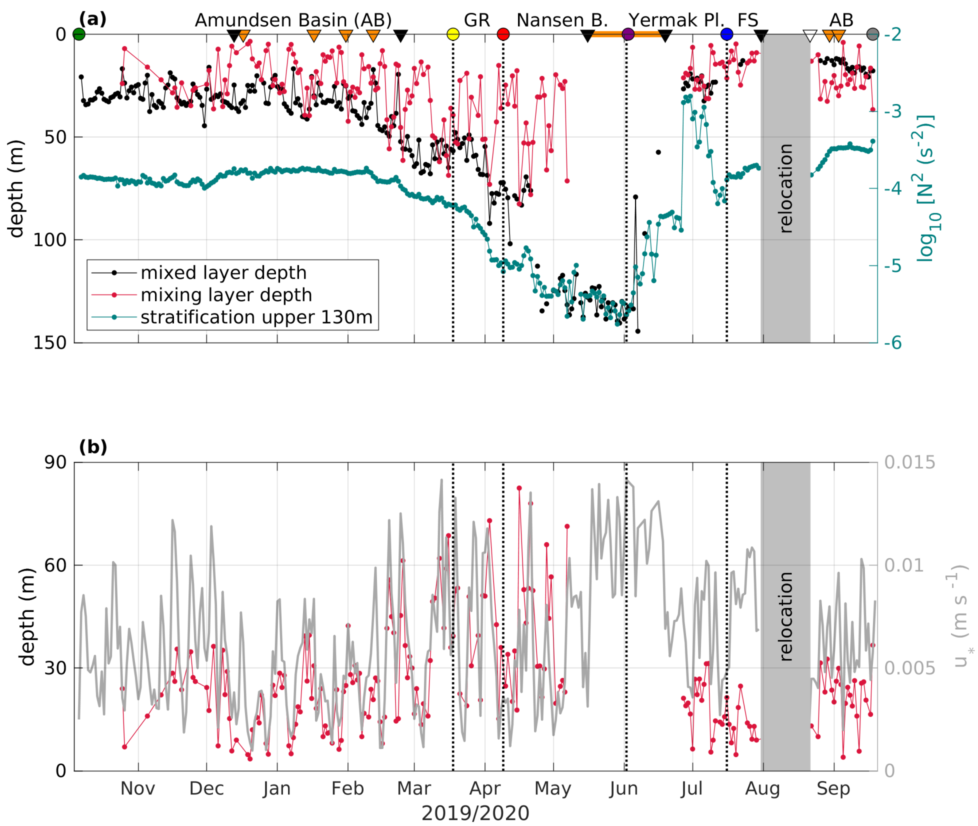

Figure 6. (a) Surface mixed layer depth (black) and mixing layer depth (red, m, left vertical axis) and upper ocean stratification (teal, right axis, s^{-2}. (b) Mixing layer depth (red, m, left axis; note that the vertical axis is reversed) and friction velocity (gray, right axis). In (a), black and white triangles indicate the start and end of the legs, dots and vertical dotted lines the geographical markers, and the orange line the uncrewed period of the drift as in Fig. 1b, and orange triangles indicate the time of the main eddies.

biological production (or consumption) in the respective layers (Carranza et al., 2018).

This relation between the depth of the mixed, and active mixing, layer is illustrated in Fig. 6a. At times, active mixing reaches down to the base of the mixed layer, but often turbulent energy already decays within the upper 20 m. In the Nansen Basin, in the presence of deep ventilation conditions, active mixing occasionally reaches down to a maximum of 80 m, but not to the mixed layer base located at $\sim$130 m. However, we have limited observations of turbulence here, due to the interruption of the drift between legs 3 and 4. Upon return to the Amundsen Basin in summer, the mixed layer depth is shallower compared to the winter condition, caused by a lower surface salinity and hence stronger upper ocean stratification (teal line, Fig. 6a). The active mixing layer depth, however, is comparable to the maximum depth of active mixing typically observed in this region in winter, during the first part of the drift, and reaches *deeper* than the mixed layer base. In other words, the same level of turbulent energy that created an approximately 30 m deep mixed layer in the presence of weaker upper ocean stratification (first part of the drift), only created a 20 m deep mixed layer in the presence of stronger stratification (last part of the drift). This illustrates how strong stratification requires more turbulent energy to be mixed, and that storm events, associated with elevated levels of turbulence, can have a different impact on the vertical transport of, e.g., nutrients and other biogeochemical compounds or organisms, depending on the strength of the upper ocean stratification.

As the turbulent energy in the mixing layer mainly originates from friction at the ice-ocean interface, the depth of the mixing layer is - to a large extent - related to the sea ice drift speed. A parameter to describe the impact of drift speed on upper ocean turbulence is the friction velocity, $u_\star$ (Fig. 6b, right vertical axis). In the (winter) Amundsen Basin and in the Nansen Basin, the evolution of the mixing layer depth corresponds to variations in friction velocity, on a daily time scale. The relationship is different, but still visible above Yermak Plateau, and breaks down in the Fram Strait. Both regions are characterized by considerably higher current velocities, which likely contribute to the friction at the ice-ocean interface. Furthermore, sea ice melt has probably reduced the bottom roughness of the sea ice (which has been kept constant in the u_* calculation here), thereby reducing the efficiency of energy transfer from sea ice drift to surface ocean turbulence. After resuming sampling on another ice floe in the Amundsen Basin in late summer, in the presence of a stronger upper ocean stratification, the mixing layer depth is relatively constant, and the effect of the friction velocity is less clear. In summary, variations in ice drift speed strongly influence the mixing layer depth on daily or probably shorter time scales, but other effects like the upper ocean stratification and tides are likely to alter this relationship.

The different timescales on which the active mixing and the mixed layer depth vary can have implications for the distribution of tracers and organisms in the near-surface layer. During longer calm periods, when the wind and drift speed are low, vertical biogeochemical gradients might be established within the surface mixed layer, e.g., if nutrients are preferentially consumed in the upper part of the mixed layer, where more sunlight is available, or if tracers and organisms from melting sea ice are injected to the ocean and accumulate only in the very top layer. A wind event can then easily homogenize these gradients on very short (hourly) timescales, altering the biogeochemical signature over the whole mixed layer depth. Such an event could boost primary productivity, by replenishing surface nutrients, but could also have an adverse effect by displacing organisms to greater depths, where less sunlight is available and food is more diluted.

6.2. Turbulent Diffusivity

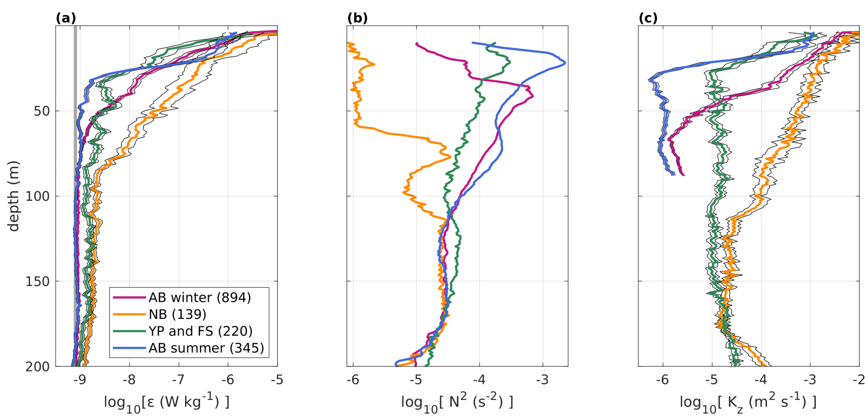

Figure 7. Basin-averaged vertical profiles of the (a) turbulent dissipation rate ε (W kg^{-1}), (b) Brunt-Väisälä frequency, N, squared (s^{-2}), and (c) vertical diffusivity K_z (m^2 s^{-1}). Black lines indicate the respective confidence levels for the average profiles. Colors refer to the different basins, the gray line in (a) indicates the lowest detection (”noise”) level of the profiler. Data below around 90 m in the Amundsen Basin (AB) and below 200 m in the Nansen Basin (NB), and the Yermak Platau (YP) and Fram Strait (FS) region are at noise level and not shown in (c).

The decay of turbulent energy with increasing distance from the surface, where it is generated mainly by friction under the sea ice, is visible in Fig. 7a. In the Amundsen Basin, strong stratification (Fig. 7b) confines elevated levels of mixing to the upper $\sim$70 m in winter, and – due to stronger surface stratification – to $\sim$50 m in summer. In the Nansen Basin, where the upper ocean is well mixed or only weakly stratified (yellow lines in Fig. 7), turbulence is elevated in the upper 90 m, and still slightly above noise level down to $\sim$200 m. The Yermak Plateau and Fram Strait region are more stratified, partly due to buoyancy input by meltwater and solar warming, but also more dynamic (see section 5). Here, turbulence is strongly elevated in the upper 40 m, and still elevated, but weaker than in the Nansen Basin, below.

Vertical diffusivity, the coefficient necessary to calculate turbulent vertical fluxes in the presence of stratification, differs both regionally and depending on the vertical position in the water column. In the strongly stratified halocline in the Amundsen Basin, values are smallest and on the order of 10^{-6} m^2 s^{-1}, as already reported in Schulz et al. (2023a), illustrating how the halocline separates the surface from the deeper water layers. In the conditions we encountered in summer, characterized by lower surface salinity and a shallower mixed layer, the "bottleneck" for vertical transport formed by the halocline is even more pronounced (blue and violet lines in Fig. 7c). In the Yermak Plateau and Fram Strait region, upper ocean (30-160 m) vertical diffusivity is an order of magnitude higher, around 10^{-5} m^2 s^{-1} (green line in Fig. 7c). In the Nansen Basin, upper ocean vertical diffusivity is highest, ranging from more than 10^{-3} m^2 s^{-1} in the upper 50 m, gradually decreasing to approximately 10^{-5} m^2 s^{-1} at around 170 m depth. Highest vertical fluxes of any tracer, e.g., heat, nutrients or oxygen, are therefore expected in the Nansen Basin.

The variability within both basins is relatively low, and average values are a good representation of the typical conditions. However, the Yermak Plateau and Fram Strait regions are very dynamic and exhibit considerably different conditions, e.g., with respect to tidal currents (section 5), stratification, and Atlantic Water layer properties (section 4). Here, average values can be informative and descriptive, but for detailed studies in those regions, the actual contemporaneous conditions need to be considered.

6.3. Heat fluxes

Ocean heat fluxes presented here were calculated in two ways. Close to the surface (3 m depth), high-resolution point measurements of three-dimensional velocity and temperature from an autonomous buoy provide heat fluxes based on direct eddy correlation methods. In deeper layers, we can derive heat fluxes from vertical temperature gradients and the vertical diffusion coefficient K_z (described above), e.g., over the halocline or the Atlantic Water thermocline (see Tab. 1, section 2, Appendix). The heat flux at 3 m reflects how small difference in heat, i.e., water even slightly above the local salinity-controlled freezing point, is transported near the ice-ocean interface. The heat flux over the halocline describes the heat entering the surface mixed layer from the ocean below. The heat flux over the thermocline can be interpreted as the heat lost from the Atlantic Water to the colder water layer above (Schulz et al., 2021). Similarly, vertical fluxes of other tracers, e.g., nutrients or dissolved oxygen, could be calculated from the K_z data presented here, and the respective tracer profiles. Depending on the position of the layer of interest, e.g., the nitracline, we expect that these fluxes qualitatively follow the variability we observe in heat fluxes.

Heat fluxes at 3 m depth, near the top of the ocean mixed layer (Fig. 8a), range between -2 and 7 W m^{-2} and exhibit a typical wide day-to-day variability, arising primarily from the variable wind-forced motion of the ice (Fig. 5a). During the winter period, in the absence of solar heating, the 3 m fluxes arise from wind-ice forced turbulent mixing of heat within the mixed layer, and heat trapped by the strong salinity-controlled density gradient at the base of the mixed layer. Heat transport from the base of the mixed layer is strongly amplified in the presence of eddies. During the ice growth period (December to end of April), ice basal growth of 0.92 m to 1.05 m was measured at the L2 floe (AOFB altimeter, Perovich et al. (under revie)). This basal growth is dominated by ice conductive fluxes controlled by air temperature, the effects of highly insulating snow, ice thickness and ice salinity. Since the ocean mixed layer temperature is very close to the freezing point (Fig. 4b in section 4.2), heat lost to the ice cannot further cool the ocean, but rather forms ice, releasing brine and removing latent heat from the ice-water interface (e.g. McPhee, 2008). The small contribution to ice basal change from time-integrated predominantly upward heat fluxes for this timeseries was just 1.2 cm of ice loss, with little contribution after the beginning of May 2020. Heat transport within the surface layer and its spatial variability across the Distributed Network is explored further in (Stanton et al., in prep).

As previously reported, based on the winter Amundsen Basin data from MOSAiC (Schulz et al., 2023a), the heat flux over the halocline is negligible, meaning that the halocline effectively shelters the upper water layers and the sea ice from the heat in the Atlantic Water layer. While there is a minimal upward flux in the Amundsen Basin in winter, though with heat fluxes much smaller than

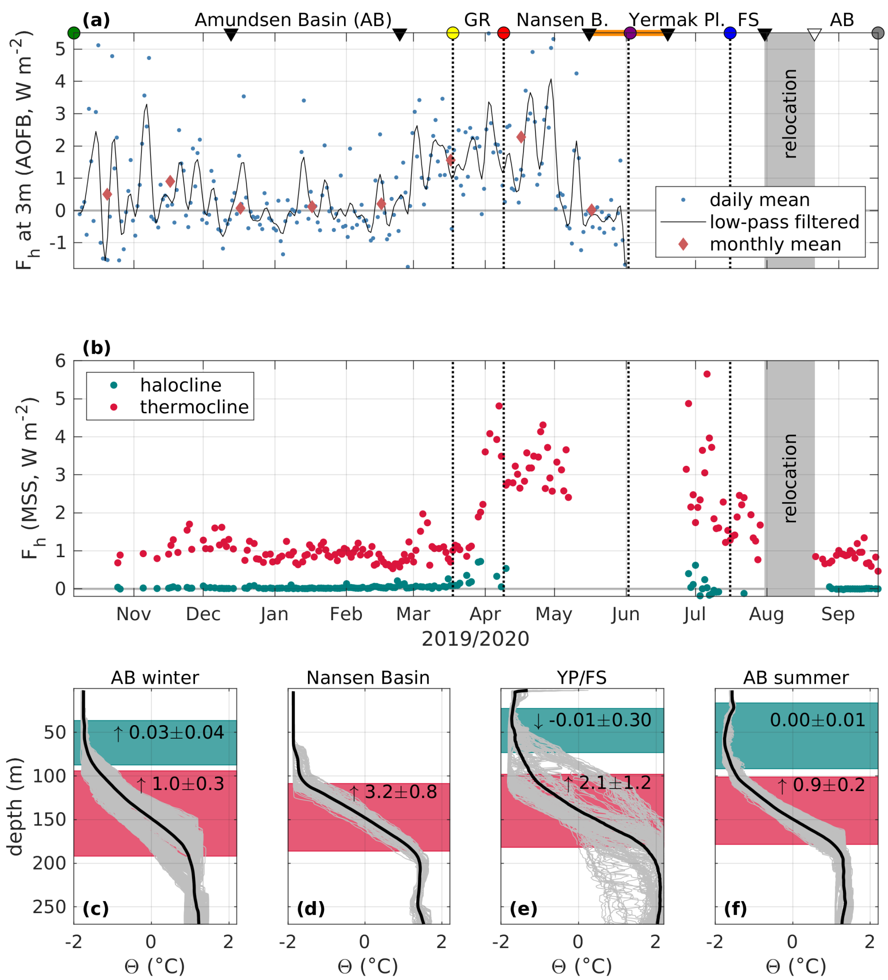

Figure 8. Vertical heat fluxes during the drift: (a) at 3 m depth, based on eddy-correlation, measured with an Autonomous Ocean Flux Buoy (AOFB) at the Distributed Network L2 site (Rabe et al., 2022), in a distance of 15–25 km from *Polarstern*. Blue dots are daily averages, the black line is a 6 day low-pass filtered timeseries, and red diamonds are monthly mean flux values. (b) Over the halocline (teal dots), and AW thermocline (red dots) based on shear probe measurements (MSS). (c)-(f) Individual (gray) and average (black) temperature profiles, and average halocline and thermocline heat fluxes in the respective basins. All values are in W m^{-2}. In (a), triangles indicate the start and end of the legs, dots and vertical dotted lines the geographical markers, and the orange line the uncrewed period of the drift as in Fig. 1b.

0.1 W m^{-2}, the stronger stratification present in summer completely suppresses any heat transport over the halocline (Fig. 8a,c,f). When approaching the Gakkel Ridge in March, halocline heat fluxes gradually increase and reach maximum levels above the ridge. However, daily mean values are still small, below 0.8 W m^{-2} (directed upwards). Halocline heat fluxes above the Yermak Plateau are comparable to those above the Gakkel Ridge, until surface heating reverses the temperature gradient, and we observe small, downward-oriented heat fluxes.

Upward heat loss from the Atlantic Water layer in the Amundsen Basin is around 1 W m^{-2}, with little (sub)seasonal variability. Under deep ventilation conditions in the Nansen Basin, in the absence of a sheltering halocline, the more turbulent surface layer directly connects with the Atlantic Water layer, and thermocline heat fluxes are increased by a factor of three, compared to the Amundsen Basin conditions with a stable halocline (Fig.8b,c,d,f). In the Yermak Plateau and Fram Strait region, heat fluxes are also enhanced, but the temperature structure in the water column - and hence the heat flux - is more variable (Fig. 8c). Here, heat fluxes are highest on the plateau, where the Atlantic Water layer is shallow and the Atlantic Water core is warmer (and younger) compared to the rest of the drift. Heat fluxes decrease to a level between Nansen and Amundsen Basin conditions when entering Fram Strait.

7. Comparison of MOSAiC data and Ocean Climatologies

Ocean climatologies are interpolations of observed temperature and salinity profiles, which are often used as initial or boundary conditions in modeling studies, or for ground-truthing the results of simulations. In contrast, state estimates are realizations of numerical models that have been optimized to best fit observational data, while obeying the physical laws that govern processes in the ocean. The majority of data used to create the climatologies were collected more than 10 years ago (Table 2), and since the Arctic is the world's fastest-changing region, it is unclear how representative these datasets still are. The high-resolution MOSAiC data serves as a benchmark for the "modern-day" Arctic, enabling us to evaluate how representative the climatologies are of the current conditions. Here, we compare four climatologies and two state estimates in three time periods/regions (Fig. 9) to the new MOSAiC data. While not entirely independent, these datasets are constructed from different data sources (see Appendix), and encompass different time periods.

Overall, we find good agreement between the climatologies and MOSAiC data, regarding the vertical structure, and seasonal and regional variability. The

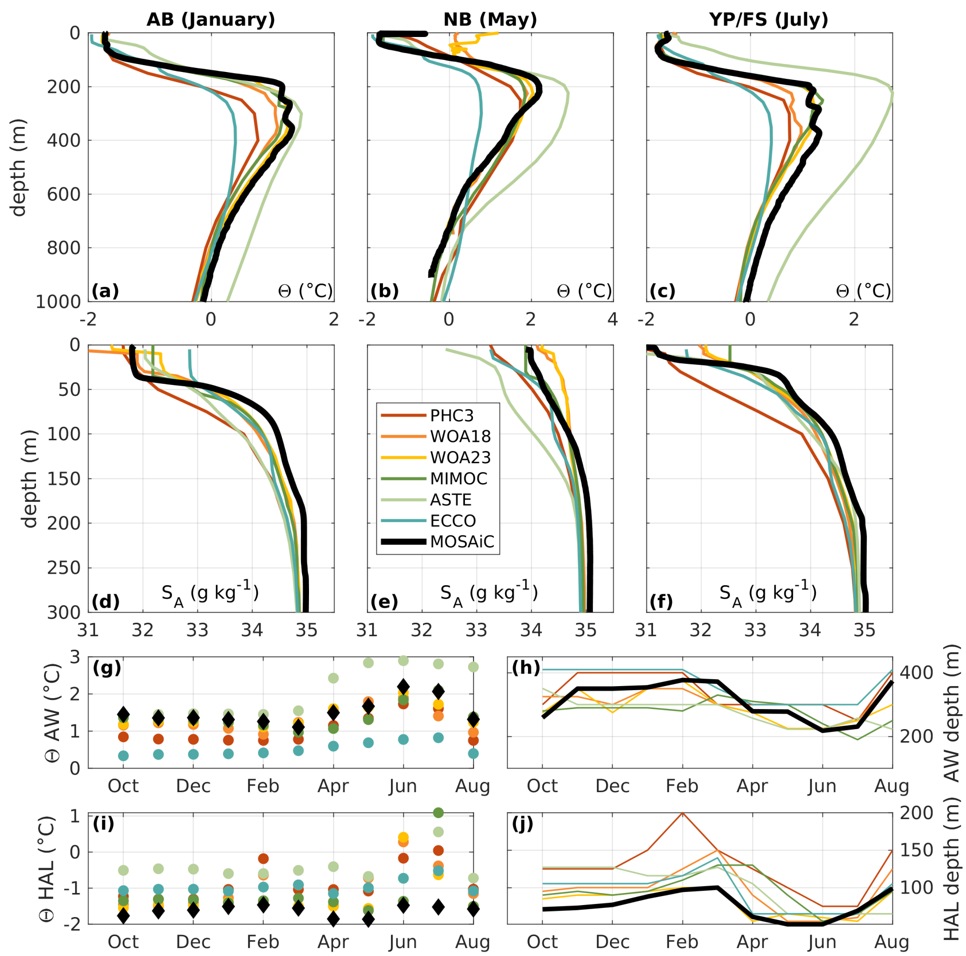

Figure 9. Comparison of (a,b,c) temperature and (d,e,f) salinity profiles of four different climatological datasets (PHC3, WOA18, WOA23, and MIMOC) and two state estimates (ECCO and ASTE, see section 2, and Appendix for details) and the MOSAiC observations. Note the different ranges on the y-axis for salinity and temperature. Data has been averaged for the months of January (Winter), May (Spring), and July (Summer), for the region covered by the MOSAiC drift during each respective period. Atlantic Water (AW) core (g) temperature, (h) depth; halocline (i) temperature and (j) depth.

MIMOC and WOA18 climatology show strong agreement and similarity, despite WOA18 containing a larger proportion of older data compared to MIMOC. The two state estimates, ECCO and ASTE, accurately reconstruct the complex vertical structure and the halocline, as well as seasonal and regional changes. Not all climatologies accurately represent the surface mixed layer, which is subject to considerable short-term variability, as profiles were often averaged over different regions and time periods. MIMOC is the only climatology that considers this issue during the interpolation and objective mapping process.

PHC3, with the oldest data of all the data products considered here (Table 2), features a fresher Atlantic layer and halocline, compared to other data products and MOSAiC data, which is expected as most data is pre-Atlantification (Polyakov et al., 2017). The state estimates ECCO and ASTE are subject to temperature biases in the Atlantic layer, with ECCO being 1-1.5°C colder, and ASTE being 0.2-2.0°C warmer (with a larger bias in spring/summer Eurasian Basin than in the winter Amundsen Basin), compared to the observed Atlantic Water core. ASTE also exhibits a salinity bias, with a fresher Atlantic Water and halocline layer, resulting in a weaker stratification. These biases point to issues reproducing the Atlantic Water pathway (a common issue in many models, e.g. Heuzé et al. (2023b); Wang et al. (2023)), an underestimation of vertical heat fluxes from the Atlantic Water layer, and not enough observations along the Eastern Arctic boundary current available to constrain the model (Nguyen et al., 2021). Constraining a new release of ASTE with MOSAiC data will likely reduce this bias.

Across all basins and seasons, the MOSAiC data consistently exhibit warmer Atlantic Water, compared to the climatologies. The climatologies demonstrate a clear temporal dependency, with PH3, containing the oldest data, featuring the coldest Atlantic Water, approximately 1°C colder compared to the most recent WOA23. This observation aligns with the expected consequences of rapid Arctic Amplification and Arctic Ocean warming (Rantanen et al., 2022). Another possible shift is indicated in the Amundsen Basin halocline properties, the extent of which decreases from 130-200 m in the (oldest) PHC3 climatology to 70-100 m during MOSAiC. This shift is in line with previous findings of a weakening and shallowing of the halocline over recent decades (Polyakov et al., 2020a). The identification of long-term variability and/or climate-change induced changes in water mass properties at all depths is not trivial. It requires in-depth analyses of variability and changes in both the upstream (e.g., properties in and exchanges with the Nordic Seas) and the internal (e.g., shelf ventilation) processes. Such analyses can only be done by comparing MOSAiC to several decades of scarce, historical data, and is beyond the scope of this study and will be the topic of future efforts.

8. Discussion

8.1. MOSAiC findings in comparison with previous results

8.1.1. Surface waters

Upper ocean properties along the MOSAiC drift were strongly influenced by the relative position of the sampling within or outside of the river water-rich Transpolar Drift. A direct comparison to earlier observations is challenging, as the exact pathway of river water is subject to seasonal and interannual variability (e.g. Mysak, 2001; Karcher et al., 2012), and sampling locations of previous expeditions or ITP drift tracks differ from the MOSAiC locations. At the beginning of the MOSAiC drift, the mixed layer salinity in the eastern Amundsen basin, around 32 g kg^{-1} (Fig. 4b), appears to be higher than in the early 2010's in the same area: Observations from late summer in 2011 (Polarstern expedition PS78, Gonçalves-Araujo et al., 2018) and 2012 (ITP64, Stedmon et al., 2021) show a fresher surface layer with salinity around 30 g kg^{-1}, and a higher CDOM loading, indicative of larger presence of river runoff in the easternmost Amundsen basin. Similar conditions were observed in 2015 (Polarstern expedition PS94, Stedmon et al., 2021)). This difference in surface salinity and CDOM concentration might indicate that the first part of the MOSAiC drift was rather intersecting the "edge" of the river water-rich Transpolar Drift, and not the core, where surface salinity would likely be closer to 30 g kg^{-1}, at least in late summer, and river water fraction would be closer to 20 % (e.g. Bauch et al., 2011; Charette et al., 2020; Paffrath et al., 2021). The conditions observed after re-location closer the the North Pole (where the core of the Transpolar Drift is often located), with surface salinities around 29 g kg^{-1} (Fig. 4b), are more typical for the core of the Transpolar Drift (e.g., Bauch et al., 2011; Charette et al., 2020). Provenance tracer data indicate that the river water component of this core is predominantly composed of Lena River water, while the smaller river water components at the "edges" are from the Yenisei and Ob rivers (Laukert et al., in prep). This is consistent with a shorter advection time of Lena River water into the central Arctic Ocean, resulting in less mixing with ambient water, and suggests significant differences in biogeochemical water properties even within the river water-influenced part of the Transpolar Drift.

8.1.2. Surface Mixed Layer Depth

Peralta-Ferriz and Woodgate (2015) report estimates of the mixed layer depth for the whole Eurasian Basin, using 519 profiles in the time period 1979–2012. Based on monthly averages, they find a maximum mixed layer depth of 73 m in April, but also observed depths of >100 m in winter, and a minimum depth of 22 m in

July/August. These ranges are similar to the conditions encountered during MOSAiC, given the high internal variability of the mixed layer depth. Peralta-Ferriz and Woodgate (2015) also highlight that the Arctic mixed layer depth distribution is patchy, and find a dominance of upper ocean stratification, rather than wind or drift speed, on determining the local mixed layer depth in ice-covered situations. Throughout the MOSAiC drift, we also find the mixed layer depth to be strongly influenced by the surface salinity, which to first order sets the upper ocean stratification. In the presence of a surface salinity below 30 g kg^{-1}, the maximum mixed layer depth is just over 20 m (Amundsen Basin, summer), whereas at a higher surface salinity of around 32 g kg^{-1}, the surface mixed layer can be as deep as 50 m. Deep ventilation, with a mixed layer depth around 130 m, was observed only at a surface salinity greater than 34.1 g kg^{-1} (Nansen Basin). Winter deep ventilation has previously been observed (Polyakov et al., 2017), and was attributed to changes associated with Atlantification, e.g. weakened upper ocean stratification, higher turbulence, and enhanced heat fluxes. MOSAiC data show that these conditions were present everywhere along the drift track in the Nansen Basin. However, a similar disappearance of the halocline, related to a high surface salinity, has already been observed in the eastern Arctic Ocean in 1990's (Steele and Boyd, 1998), and was found to be transient (Boyd et al., 2002).

8.1.3. Halocline Thickness and Stratification

Based on 18,000 profiles of ocean temperature and salinity collected between 1997–2008, Bourgain and Gascard (2011) assessed properties of the Arctic halocline. Similar to the variability encountered during MOSAiC, they found the strongest, i.e., most stratified, halocline layers close to the fresh water sources at the Siberian shelves. The weakest haloclines (together with deepest mixed layers, down to 70 m) were found in the Western Nansen Basin, where we encountered a deeper mixed layer and a complete absence of the halocline during MOSAiC. Bourgain and Gascard (2011) found the halocline in the Amundsen Basin to be very stable during their investigated time period, with no clear seasonal variability, but their data coverage in winter was sparse. During MOSAiC, we find an apparent seasonal signal, with a thicker (76 ± 9 m vs. 50 ± 11 m) and more stratified ($50 \pm 7 \times 10^{-5}$ s^{-2} vs. $28 \pm 8 \times 10^{-5}$ s^{-2}) halocline in summer, compared to the winter situation, which is attributed to a lower surface salinity in summer. However, while seasonal meltwater in the surface layer has an effect on the surface salinity, MOSAiC data indicate that it is the relative position within or outside the river-water influenced Transpolar Drift, rather than seasonality, which sets the local surface salinity (see section 4). Taking into account both seasons, the Amundsen basin halocline got thinner (55 ± 14 m vs. 70 ± 10 m) but more stratified ($32 \pm 12 \times 10^{-5}$ s^{-2} vs. $20 \pm 3 \times 10^{-5}$ s^{-2}) compared to the values reported in Bourgain and Gascard (2011). Given the strong spatial gradients in surface salinity in the Amundsen Basin, and the still limited spatial coverage of data, these differences could reflect internal variability rather than trends.

8.1.4. Heat Fluxes

Heat fluxes near the ice-ocean interface (at a depth of 3 m) exhibit low values during the MOSAiC winter and display significant day-to-day fluctuations. This pattern aligns with the findings of Meyer et al. (2017a) in the Nansen Basin during the N-ICE winter (at 1 m depth). Moving into early spring, specifically in May, the heat fluxes recorded by the AOFB buoy reached levels of around 5 W m^{-2}, a value that is consistent with the approximately 10 W m^{-2} reported by Meyer et al. (2017a) for the same month. In June, during the N-ICE campaign, the fluxes ranged between 10-50 W m^{-2}, reaching peaks exceeding 300 W m^{-2} during storms that caused upward mixing of warm subsurface waters. Unfortunately, the MOSAiC data lacks shallow measurements from June onwards.

Heat fluxes across the halocline during MOSAiC are very small, which is in line with previous findings (Fer, 2009), also from the SHEBA campaign in the Western Arctic (Shaw and Stanton, 2014). Also, the relatively low heat fluxes over the Atlantic Water thermocline found in Amundsen Basin match previously reported values in that region (Lenn et al., 2009; Schulz et al., 2021). The higher heat fluxes over the thermocline found in the Nansen Basin correspond to values of around 3 W m^{-2} found during N-ICE in 2015 Meyer et al. (2017a), and elevated heat fluxes in the absence of a halocline - as observed in the Nansen Basin - have previously been reported (Steele and Boyd, 1998). Heat fluxes over the thermocline for June and July were generally confined to the range of 2-5 W m^{-2}; much lower than during N-ICE. This is primarily attributed to the shallower warm Atlantic layer in the N-ICE area compared to the MOSAiC location, and the absence of storms during this period of the MOSAiC drift.

8.2. Interdisciplinary Implications

The regional differences in hydrography encountered during the MOSAiC drift have various implications for other Arctic subsystems. In the following, we discuss how the variability in physical properties along the MOSAiC drift might shape the distribution of nutrients and the carbonate system, bio-optical properties, the ecological structure on different trophic levels, and sea ice and atmospheric processes.

8.2.1. Nutrient and carbonate system dynamics

The most direct connection is probably the effect of water mass and transport pattern variability on the distribution of chemical components, such as nutrients and carbon. Nutrient inventories in the surface waters differ regionally, with signals being potentially larger than the seasonal signals of biological uptake and remineralization (Juranek, 2022), particularly in basins with longer ice-cover duration where the residence time of tracers is increased due to accumulation in surface waters (Eveleth et al., 2014) . Similarly, for various carbonate system components, such as dissolved inorganic carbon (DIC) and total alkalinity (TA), a strong positive correlation is usually found with salinity (Friis et al., 2003), indicating that the marine carbonate system is closely related to physical water mass properties.

Atlantic Water, residing at depths greater than 100 m, forms the largest source of nutrients in the Central Arctic Ocean and is an enormous reservoir of dissolved carbon, as organic matter from the sun-lit surface ocean eventually sinks and remineralizes. The transport of these nutrients and carbon up to the photic zone - where they can be utilized by primary producers - is strongly limited by the presence of the halocline, which acts as a barrier layer (e.g., Fer, 2009; Schulz et al., 2022a). When the halocline is absent and the mixed layer penetrates the Atlantic Water layer (Polyakov et al., 2017), ventilation can potentially create locally larger nutrient inventory at the start of the productive season, and enhance the biological carbon drawdown (Juranek, 2022). This is observed in the Nansen Basin (section 4.2). Enhanced vertical nutrient transport might also occur when Atlantic Water resides high up in the water column (Yermak Plateau, section 4.3). On the other hand, vertical mixing of deep DIC during ventilation or passing eddies, can partially offset biological CO_2 drawdown by increasing the partial pressure of CO_2 (pCO_2) in the surface layer (Bates and Mathis, 2009; Lannuzel et al., 2020).

Among marine carbonate system components, the surface layer pCO_2 is often the point of focus in sea-air CO_2 exchange studies, as it determines whether the ocean is a sink or source of CO_2 to the atmosphere. The Arctic Ocean is generally considered to be a CO_2 sink, as surface layer pCO_2 is often undersaturated relative to the atmosphere (Tanhua et al., 2009; Schuster et al., 2013; Fransson et al., 2017; Rogge et al., 2023). Arctic Ocean pCO_2 undersaturation is driven by low seawater temperatures, sea ice meltwater input, biological CO_2 uptake during the summer, and strong upper ocean stratification (Bates et al., 2006; Takahashi et al., 2009; Fransson et al., 2017). In addition to the variability in the Arctic Ocean's nutrient content and capacity to absorb atmospheric pCO_2 driven by biogeochemical and sea ice processes, physical processes also can lead to changes in the marine nutrient and carbonate system on short time scales. For example, frontal regions are associated with enhanced biological activity, leading to variability in uptake and remineralization rates of nutrients across smaller hydrographic scales (Eveleth et al., 2014). Tidal currents in regions where horizontal gradients of water masses exist, e.g., between Yermak Plateau and Fram Strait, can also lead to rapid change in the nutrient and carbonate system of the surface ocean on semidiurnal and diurnal time scales, and cause polar waters to switch between a CO_2 sink and source multiple times a day (Skogseth et al., 2013; Llanillo et al., 2019; Droste et al., 2022).

8.2.2. Optical properties

The optical properties of the surface waters exhibit regional differences between the basins, exemplified by the documented differences in CDOM concentrations, with elevated concentration when in the Transpolar Drift (see section 4.2). In Arctic waters, CDOM is an important factor of light attenuation in the water column (e.g. Hill, 2008; Granskog et al., 2007; Pavlov et al., 2015), and varies regionally, largely depending on the presence of river water. This divides the Eurasian basin in bio-optical provinces (Gonçalves-Araujo et al., 2018), which can have an effect on the light availability for primary producers (e.g. Pavlov et al., 2015), especially in the absence of sea ice. Solar heating of the upper ocean is also affected by the distribution of CDOM (Hill, 2008; Granskog et al., 2015), and could thus affect sea ice melting across regimes.

8.2.3. Ecology

Regional variability in both the nutrient concentration and the optical regime can induce structural changes to the microorganism community, with complex implications for the carbon biogeochemistry. For example, increased vertical transport of nutrients from the deep ventilation observed in the Nansen Basin could lead to a shift from smaller to larger phytoplankton, while increased stratification and warming leads to opposite trends (Li et al., 2009; Morán et al., 2010). Additionally, hydrographic boundaries can act as physical barriers limiting dispersal, resulting in vertical and biogeographic differences in microbial diversity and community structure among water masses and basins (Galand et al., 2010; Han et al., 2015). During MOSAiC, unique upper water column microbial community compositions were indeed observed when crossing boundaries such as the base of the mixed layer, or when drifting into and out of the Transpolar Drift as described here (Chamberlain et al., in prep). A key driver in regional differences in Arctic Ocean bacterial communities is the relative proportion of Atlantic water influence, with Species composition and ecological function, i.e., substrate utilization, responding rapidly to changes in the environmental regime. This connection makes the variability in water masses, for example the high relative proportion of Atlantic water observed while crossing the Yermak Plateau, a key driver in regional differences of microbial communities (Carter-Gates et al., 2020; Priest et al., 2023). At higher trophic levels, Atlantic species enter the Arctic Ocean within the Atlantic Water layer, and appear to survive in parts of the central Arctic. During MOSAiC, healthy Atlantic cod were found in the Amundsen Basin, where a deep scattering layer indicates the presence of living organisms as food supply (Snoeijs-Leijonmalm et al., 2022). In the Nansen Basin, this deep scattering layer was absent, and fish and squid abundance decreased. The inflow region of young Atlantic Water near Yermak Plateau, on the other hand, was characterized by large aggregations of Atlantic fish species (Snoeijs-Leijonmalm et al., 2022).

8.2.4. Sea ice and atmosphere

Oceanic heat - when reaching the surface - has an effect on sea ice growth and melt. During MOSAiC, the sea ice basal growth was found to transition from a rapid to a slower growth rate, when drifting from Amundsen Basin to Nansen Basin (Lei et al., 2022). This change in basal growth rate might be, to some extent, related to the greater vertical heat transport from the Atlantic Water layer in the Nansen Basin, associated with the deep ventilation conditions (absence of the halocline). During the melt season, elevated ocean surface temperatures contribute to sea ice melt, and small vertical gradients in upper ocean temperature might set different melt rates at, e.g., the keels of ridges (Salganik et al., 2023b). The presence of shallow, strongly stratified meltwater layers also affects the sea-ice melt rates (Salganik et al., 2023a; Smith et al., 2023). Indirectly, even atmospheric conditions might be influenced by surface ocean conditions, by affecting the emission of marine aerosol precursors that play an important role in, e.g., cloud formation (Schmale et al., 2021).

9. Summary

For this study, we compiled a quality-controlled dataset of temperature and salinity profiles, and derived parameters, with the best available temporal coverage along the whole MOSAiC drift across the Eurasian basin in 2019/2020. Derived core parameters based on this dataset (Schulz et al., 2023b; Mieruch, 2023) can be used for interdisciplinary studies aiming to understand interactions between ocean physical properties and a large range of other measurements conducted during MOSAiC. Along with other ocean data presented here, we find that from an ocean perspective, MOSAiC was rather a transect across the Eurasian basin than a time series primarily reflecting a seasonal evolution. Considerable gradients in the surface waters are present, related to the MOSAiC ice camp drifting into and out of the river water influenced Transpolar Drift in the Amundsen Basin. In the Nansen Basin, high surface salinity and the associated absence of the halocline allows for a more direct connection and enhanced exchange between the surface and deeper waters of Atlantic origin. Further south, above Yermak Plateau and in the Fram Strait, oceanic conditions were more dynamic, with a pronounced regime shift back into surface waters with a high fraction of terrestrial water when leaving Yermak Plateau. This spatial variability likely has large implications for the ocean biogeochemistry, ecology, and even sea ice and atmospheric conditions observed during MOSAiC.

Appendix: Details on Instrumentation and Methods

Parameter	**Unit**	**Source**
time	UTC	Polarstern/CO1 GPS buoy
position	degree	Polarstern/CO1 GPS buoy
water depth	m	IBCAO
drift speed	m s^{-1}	position data
conservative temperature profile Θ	°C	CTD and MSS/ITP and PGO4
absolute salinity profile S_A	g kg^{-1}	CTD and MSS/ITP and PGO4
mixed layer depth	m	CTD and MSS/ITP
surface conservative temperature Θ	°C	CTD and MSS/ITP and PGO4
surface absolute salinity S_A	g kg^{-1}	CTD and MSS/ITP and PGO4
surface freezing point	°C	from surface Θ and S_A
friction velocity u_*	m s^{-1}	drift speed
mixing layer depth	m	MSS
heat flux halocline	W m^{-2}	MSS
heat flux thermocline	W m^{-2}	MSS

Table 4. Parameter in the daily average dataset.

Drift Track, Speed, and Bathymetry

Positioning data along the drift track is taken from *Polarstern* during the times when the ship was anchored to the floe, at 10-minute resolution, and from the Central Observatory CO1 GPS buoy, during the transit time of the exchange between legs 3 and 4, at 1-hour resolution. The drift speed was calculated based on the full resolution of the position dataset. From the (complex) ice drift velocity U, we can calculate the friction velocity u_* using the Rossby similarity equation (McPhee, 2008), as already done for parts of the MOSAiC data in Kawaguchi et al. (2022):

$$\frac{U}{u_*} = \frac{1}{\kappa}\left(\log\frac{u_\star}{fz_0} - A \mp iB\right), \tag{1}$$

where $\kappa = 0.4$ is the von Kárman constant, $A = 2.3$ and $B = 2.1$ are constants (McPhee, 2008), $z_0 = 0.01$ m is the hydraulic roughness, and f is the Coriolis frequency.

Bathymetric data is extracted from the IBCAO v4.2 400 m resolution bathymetric dataset (Jakobsson et al., 2020) along the full resolution drift track, and available from the deep CTD casts, as the sum of water depth and altimeter-based distance to the sea floor. In addition, we use the *Polarstern* scientific echosounder (SIMRAD EK60) data to calculate the true water depth according to the following procedure: One-minute means of the 18kHz channel were extracted from the dship database and merged with the ship's GPS position. The uncorrected depth time series data were plotted on true water depths obtained by full-depth CTD casts, resulting in a mismatch on the order of 50 m. This mismatch is generally the result of a deviation of the sound speed the instrument was configured to and the actual integrated sound speed in the water column. The EK60 was most of the time configured to a sound speed of 1500 m s^{-1}, but this configuration was occasionally changed and not documented. To obtain more accurate depths, depth-dependent true sound speed was calculated using full-depth CTD profiles. Additional corrections were performed for three periods where the sound speed in the instrument configuration was presumably changed. These periods were November 25 to 28, 2019 (instrument presumably configured to 1470.2 m s^{-1}), May 26 to August 15, 2020 (instrument presumably configured to 1440 m s^{-1}), and August 15, 2020 to end of expedition (instrument configured to 1472 m s^{-1}). An additional anomaly between August 26 and September 12, 2020, was also corrected. Finally, a moving median filter with a window size of 5 hours was applied to remove spikes. The resulting data matches the available true CTD water depths within 10 m.

Temperature and Salinity profiles

Temperature and salinity data used in this study are taken from five different sources: The *Polarstern* CTD (Tippenhauer et al., in reviewb), the Ocean City CTD (Tippenhauer et al., in reviewa), a microstructure profiler (Schulz et al., 2023c), ice-tethered profilers (ITPs) (Toole and Krishfield, 2016), and a CTD chain (Hoppmann et al., 2022b). The *Polarstern* CTD is an SBE911plus system, with 24 Niskin bottles (12 liters each) attached for water samples at different depth. It was operated from the side of the ship. Here, we exclude casts that were performed during transit periods, and two profiles (from July 23 and 30, 2020) that showed potentially unrealistic data. The Ocean City CTD is the same SBE911plus system in a smaller frame, featuring 12 Niskin bottles (5 liters each), and was operated through a hydrohole in some distance to *Polarstern*, during legs 1-3. We exclude one suspicious profile on January 7. Details on the processing of both CTD datasets can be found in Tippenhauer et al. (in prep). Through the same hydrohole in Ocean City, upper ocean profiles with a free-falling microstructure profiler (MSS) were obtained on a near-daily basis. In addition to temperature and salinity measurements, the MSS is also equipped with shear probes, that allow to sample the small-scale, chaotic motions in the water, from which the turbulent dissipation rate ε (W kg^{-1}) can be derived. Details on the processing can be found in Schulz et al. (2022b). From the original MSS dataset, we exclude casts that terminate within the upper 100 m of the water column, or exhibit unrealistic behavior in one of the data channels (casts IDs 23, 220, 442, 4047, 4233, 8202, based in Tab. 1 in Schulz et al. (2022b)), and any profiles obtained during transit, i.e. after September 20, 2020. On days without any CTD or MSS profiles, mostly between legs 3 and 4 (May 15 to June 27), we include data from the ice-tethered profilers ITP94 (up to one profile per day, 10 profiles were not used due to questionable data quality) and ITP111 (up to two profiles per day). These systems consist of a surface buoy, including a data transmission system, attached to a cable on which the actual profiler moves up and down (Krishfield et al., 2008; Toole et al., 2011), and were deployed on floes in the vicinity of the central observatory at the start of the MOSAiC drift (Rabe et al., 2022). The ITP data is archived as in-situ temperature and practical salinity, and was converted to Conservative Temperature and Absolute Salinity for this study, using the TEOS10 Gibbs-SeaWater Oceanographic Toolbox (McDougall and Barker, 2011). Some of the ITP profiles only start at several 100 m depths, leading to the gaps visible in the dataset (Fig. 2), and did often not start shallow enough to allow for deriving surface layer properties. Hence, we also include daily averaged data from the Pacific Gyre buoy OG O4 (Hoppmann et al., 2022a) on days without CTD and MSS measurements. These buoys consist of five SBE37IMP MicroCAT CTDs, recording (transmitting) temperature and salinity data every 2 minutes (10 minutes) at depths of 10, 20, 50, 75, and 100 m. Data from the uppermost MicroCAT are used to fill in gaps in the daily surface temperature and salinity data. Altogether, the here presented dataset includes 2434 individual profiles of Conservative Temperature Θ and Absolute Salinity S_A, on in total 325 days, covering the period between October 6, 2019 to September 18, 2020, with a break between July 31 and August 21, 2020 due to relocation north.

Cross-Calibration and Quality Control

To ensure the quality of the combined dataset, we compare data from each instrument to the Polarstern and Ocean City CTD data, which provide the only *in-situ* calibrated measurements of salinity (Tippenhauer et al., in prep). As casts of two different instruments were rarely co-located, this comparison can only be done statistically, i.e. by comparing as many as possible pairs of casts closest in time.

Most datasets are found to agree well, with the exception of the MSS casts performed with the profiler MSS055, which was mostly used during leg 3 and was equipped with a substitute conductivity sensor. For this probe, a calibration cast was performed with the MSS attached to the Ocean City CTD on February 2, 2020, which showed a constant offset in conductivity of 0.11 mS cm^{-1} (data not shown). After reprocessing the affected data with this offset correction, values were in good agreement with the CTD data.

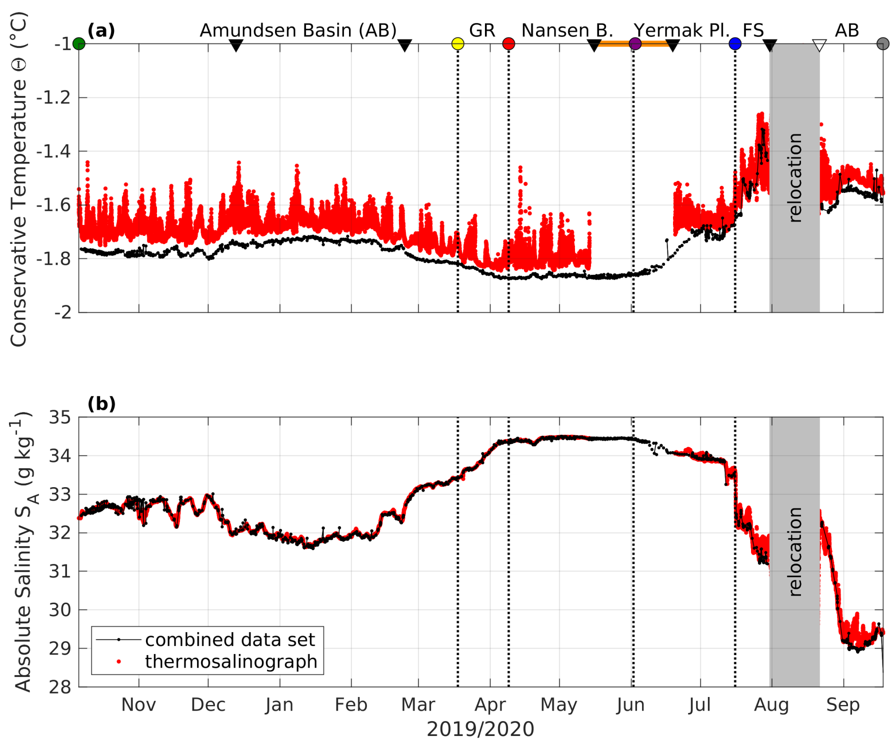

Figure 10. Time series of surface (a) Conservative Temperature (°C) and (b) Absolute Salinity (g kg^{-1}, derived from the full resolution combined dataset presented in this study (black lines) and the Polarstern thermosalinograph (red dots). In (a), triangles indicate the start and end of the legs, dots and vertical dotted lines the geographical markers, and the orange line the uncrewed period of the drift as in Fig. 1b.

The *Polarstern* thermosalinograph, an on-board system that continuously samples surface waters through an inlet in the ship's hull, is found to give unrealistic temperature data and is therefore not included here (Fig. 10a). As the presence of the ship itself raises the temperature in adjacent waters, especially on the lee side, i.e. during times of drift in the direction opposite to the thermosalinograph inlet, recorded temperatures are too high and too variable and should not be used for analysis. Salinity data is not affected and is mostly in good agreement with data from other sources (Fig. 10b). However, in the presence of considerable salinity gradients in the surface layer during the melt season, also salinity data should be treated with care, as it is unclear which effect mixing around the ship has on the water properties.

Mixed Layer Properties

The depth of the surface mixed layer is commonly calculated based on a density threshold criterion, i.e., identified as the first depth where the density increases exceed a predefined value, compared to the value at the surface (e.g., Toole et al., 2010). In this study, we calculate the surface reference potential density as the average of the upper 4-10 m, which excludes the shallow meltwater layers in summer and data points where conductivity sensors were not fully adjusted in winter. We do not calculate mixed layer depth from the discrete depth data of the CTD chain (86 profiles), or any profiles starting below a depth of 10 m (79 out of 2434 profiles, all from ITPs). We also exclude profiles that show a strong upper ocean (4-10 m) stratification of $N^2 > 3 * 10^{-5}$ s^{-2}, which is by definition not a "mixed" layer (264 profiles), indicated as purple crosses in Fig. 4a.

In the remaining profiles, we found that applying any density difference threshold between 0.04-0.08 kg m^{-3} yields similar mixed layer depths within a range of 2 m (1139 profiles), or 6 m (292 profiles, mostly in winter when salinity increases associated with brine are present at the base of the mixed layer). For these profiles, we chose the shallowest value, corresponding to a density threshold of 0.04 kg m^{-3}, as the base of the mixed layer. In the presence of a less sharp pycnocline, i.e., when the increase in density below the surface mixed layer is more gradual and mixed layer depths based on the different density thresholds differ by 6-12 m, we chose the center of the pycnocline, corresponding to a density threshold of 0.06 kg m^{-3}, as the base of the mixed layer (155 profiles). For 419 profiles, the surface mixed layer depth could not be calculated based on the above described method, and therefore no estimate is given. Previous studies using MOSAiC data applied a density difference threshold of 0.1 kg m^{-3} (Schulz et al., 2023a; Fer et al., 2022), or 0.05 kg m^{-3} (Rabe et al., 2022). In the presence of a well-defined mixed layer, the exact choice of density threshold does not matter (see above), however, it is important to apply vigorous quality control in addition to the automatic detection of mixed layer depth based on a density threshold, to exclude any estimates for profiles without a clear defined mixed layer.

Surface salinity and temperature (Fig. 4b) are calculated per profile as the average over again 4-10 m, even if the surface layer was stratified (see above), and subsequently averaged per day. Corresponding freezing point temperature was calculated using the TEOS-10 set of equations (McDougall and Barker, 2011).

River water fraction and CDOM

We quantify meteoric and sea ice-related freshwater sources based on salinity and δ^{18}O following Östlund and Hut (1984), using the following mass balance:

$$f_{\text{mar}} + f_{\text{r}} + f_{\text{SIM}} = 1 \tag{2}$$

$$f_{\text{mar}} * S_{\text{mar}} + f_{\text{r}} * S_{\text{r}} + f_{\text{SIM}} * S_{\text{SIM}} = S_{\text{meas}} \tag{3}$$

$$f_{\text{mar}} * O_{\text{mar}} + f_{\text{r}} * O_{\text{r}} + f_{\text{SIM}} * O_{\text{SIM}} = O_{\text{meas}}, \tag{4}$$

where f_{mar}, f_{r}, and f_{SIM} are the fractions of marine water, river runoff, and sea-ice meltwater, respectively, and S_{mar}, S_{r}, S_{SIM}, O_{mar}, O_{r} and O_{SIM} are the corresponding salinity and δ^{18}O values (Tab. 5). Meteoric water in the Arctic consists mainly of river runoff from the large Siberian rivers, and also contains local precipitation, with similar isotopic composition due to their common source. For simplicity, meteoric water refers to river water in this study. The main marine source in the Arctic Ocean are Atlantic-derived waters, and Pacific-derived waters that enter the Arctic Ocean via Bering Strait play no role within our sampling region (Paffrath et al. (2021), MOSAiC findings).

Table 5. End-Member Values Used in Mass Balance Calculations.

End-Member	**Salinity**[a]	**δ^{18}O (‰)**
f_{mar}	34.92±0.05	0.3±0.1
f_{r}	0	-20±1
f_{SIM}	4±1	-2[b]+2.6±1

[a]In this analysis only, practical salinity was used.
[b]Average surface water value for the central Arctic Ocean.

A negative sea-ice meltwater fraction f_{SIM} reflects the amount of water removed by sea-ice formation, and the absolute value is proportional to the subsequent addition of brine to the remaining water. The sea-ice meltwater fraction does not include meltwater from ice formed from river water, which is accounted for in f_{r}. All fractions are net values reconstructed from the δ^{18}O and salinity signature of each sample. Resulting from analytical errors, an uncertainty for each fraction of up to $\pm 0.2\%$ and $\pm 0.4\%$ is estimated associated with measurement precision for δ^{18}O analysis between $\pm 0.04‰$ and $\pm 0.07‰$. An additional systematic error depends on the exact choice of end-member values. When end-member values are varied within the estimated uncertainties (Tab. 5), both fractions are shifted by up to $\sim 1\%$, but results are always qualitatively conserved even when tested with extreme end-member variations (see Bauch et al., 2011, for details). In Fig. 4c, we show average values of river water fraction f_{r} within the upper 15 m. Sea-ice meltwater fraction f_{SIM} are not presented and discussed here, as surface layer values alone cannot be interpreted directly, e.g., in seasonal succession, but need to be interpreted in relation to deeper layers to account for local versus advective signals, which is beyond the scope of this study.

Colored dissolved organic matter (CDOM) presents another potential, qualitative tracer for river runoff in Arctic waters (e.g. Granskog et al., 2007; Gonçalves-Araujo et al., 2016; Stedmon et al., 2021), as this material originates primarily from terrestrial runoff. Here, we use CDOM data from ITP94, which was equipped with a CDOM fluorescence sensor, that detects humic-like CDOM. Values are reported in factory-calibrated units (Quinine Sulphate equivalents, ppb). During postprocessing, data is despiked using a fourth-order median filter, and data in the upper 0-15m depth is averaged for each profile.

Water Mass Definition

Here, we define the surface mixed layer down to the bounding pycnocline as described above. Below the surface mixed layer, the halocline starts, and ends when vertical stratification is also affected by changes in temperature, at a density ratio of

$$R = \frac{\alpha \Delta \theta}{\beta \Delta S} = 0.05, \tag{5}$$

where α is the thermal expansion and β is the haline contraction coefficient, following (Bourgain and Gascard, 2011). If this criterion yields a halocline layer of a thickness less than 10 m, we do not identify these waters as part of the halocline. Below the surface layers, we identify (non-modified) Atlantic Water as temperatures $\Theta > 2°$C, and (modified) Arctic Atlantic Water as temperatures $0 < \Theta < 2°$C (Rudels et al., 2012), and deeper water layers as summarized in Tab. 1. There, $\sigma_{0.5}$, σ_1, and $\sigma_{1.5}$ refer to the potential density referenced at 500, 1000 and 1500 m depth, respectively.

Current Velocity

Horizontal ocean currents are measured from the drifting sea ice, using a longrange RD-Instruments 75 kHz ADCP (Acoustic Doppler Current Profiler), deployed pointing downwards through a hydrohole (Baumann et al., 2021). The vertical resolution of the 20-minute time-averaged profiles is 8 m. Due to the unreliability of magnetic compasses at high latitudes, a GPS compass was used, and the current profiles were recorded in beam coordinates. Geo-referenced, eastward and northward velocity components in the upper 500 m were obtained during post-processing.

Barotropic, i.e., depth-mean, tidal currents along the drift were estimated from the Arctic Ocean Inverse Tide Model (AOTIM) on a 5 km horizontal grid (Arc5km2018) (Erofeeva and Egbert, 2020). We use the 8 main constituents (M_2, S_2, N_2, K_2, K_1, O_1, P_1, Q_1) and 4 nonlinear components (M_4, MS_4, MN_2, and $2N_2$) here. We also estimate the barotropic tidal current from the above-mentioned ADCP data. As our current observations were obtained from a drifting ice floe, the time series exhibit a combination of temporal and spatial variability, making it inappropriate to employ standard tidal harmonic analysis. Similar to Meyer et al. (2017a), we apply a complex demodulation as a method to isolate the tidal signals. Rotary component amplitude and phase of the diurnal and semidiurnal tides were estimated at 24 and 12 h frequencies using 48 hour long segments. It has to be kept in mind that in the Arctic Ocean, the inertial frequency is close to the semidiurnal band, and inertial oscillations will contaminate the tidal estimates (for the clockwise rotary component).

Eddies are identified visually in the ADCP data, only considering structures that appear more than in three consecutive vertical levels and at least three continuous measurements in time.

Turbulence and Heat Fluxes

Profiles of turbulent dissipation rates ε (W kg^{-1}) at 1 m vertical resolution were obtained with a free-falling, tethered microstructure profiler MSS90L, Sea & Sun Technology, Germany), through a hole drilled in the sea ice, at a minimum distance of 250 m from *Polarstern*. Details on the measurement setup and processing can be found in Schulz et al. (2022b). Based on these data, the depth of the surface active mixing layer was identified when surface-elevated dissipation rates first fall below a threshold of $\varepsilon = 5 \times 10^{-9}$ W kg^{-1}, and remain below threshold for at least three consecutive depth levels.

The vertical diffusivity K_z (m^2 s^{-1}) is calculated from ε and density profiles following Bouffard and Boegman (2013), accounting for possibly different turbulent regimes and stratification ranges. Averages of turbulent quantities, such as ε and K_z are calculated using the maximum likelihood estimator MLE (Baker and Gibson, 1987). Vertical heat fluxes are calculated from K_z values and the bulk vertical gradient (over the depth range of the respective vertical layer, halocline or thermocline, see Tab: 1) in potential temperature $\frac{\partial \theta}{\partial z}$, according to

$$F_h = -\rho_0 c_p K_z \frac{\partial \theta}{\partial z}, \tag{6}$$

where $\rho_0 = 1027$ kg m^{-3} is the reference density, and $c_p \approx 3,991.9$ J kg^{-1} K^{-1} is the specific heat capacity of sea water (e.g., Schulz et al., 2021). Positive values indicate upward heat fluxes. Heat fluxes were calculated individually per profile and then (arithmetically) averaged per day.

In addition, heat flux timeseries at 3 m depth were measured by four Autonomous Ocean Flux Buoys (AOFBs) deployed in October 2019 at the CO and three L-sites in the distributed network (see Rabe et al., 2022, for details on the distributed network), initially about 15 km from the CO. At 3 m depth, the AOFBs sampled 2Hz timeseries of high resolution 3D velocity components, temperature, and conductivity co-located in a 15 cm cube volume. Eddy-correlation heat, salt and momentum fluxes were derived from 35 minute ensemble co-spectra sampled every 2 hours. An upward-directed acoustic altimeter measured local basal ice base changes. Data from all sensors are returned to a server via an Iridium modem each day, and the buoys typically survive 6–24 months using a mix of primary batteries, solar power and wind power. In this analysis here, the heat fluxes from the longest surviving MOSAiC AOFB, at the distributed network site L2 are presented.

Climatologies

The climatologies and state estimates used in this study (Tab. 2) have significant overlaps in terms of data; however, they cover slightly different periods, contain different types of data from various sources, and are produced using distinct methods and interpolation procedures. It is important to note that historical data for the winter period in the Arctic Ocean is scarce; most Arctic Ocean cruises are conducted during the summer, leading to a bias in the climatologies towards the summer season. Additionally, the majority of Ice-Tethered Profilers (ITPs) that provide winter data in recent decades are concentrated in the western part of the Arctic and the Transpolar drift, and limited to the upper 1000 m. Due to the spatial and temporal distribution of MOSAiC data, conducting a comprehensive seasonal comparison with climatologies proves challenging. To address this, we have calculated month-long basin-wide averages for specific periods: January in the Amundsen Basin for winter, May in the Nansen Basin for spring, and July in the Fram Strait region for summer. These averages were derived from the objectively analyzed monthly fields of each climatology.

Nansen (1902) provided the first oceanographic measurements of the Central Arctic Ocean from 1893 to 1896. However, systematic oceanographic observations only began in the 1930s. During the 1980s and 1990s, the increased use of icebreakers and submarines resulted in a significant increase in hydrographic data. The bulk of historical data before 2000 was gathered to construct climatological atlases of the Arctic Ocean by the Environmental Working Group (1997), which are all included in the PHC3 climatology (Steele et al., 2001). The PHC3 climatology was, however, not updated since the early 2000s. More recent data on the Arctic Ocean is available in the World Ocean Database (Boyer et al., 2013) and the Unified Database for Arctic and Subarctic Hydrography (UDASH) dataset, which is a collection of quality-controlled profiles (Behrendt et al., 2018). As the UDASH profiles are scattered, we use the WOA18 climatology (Locarnini et al., 2018; Zweng et al., 2018) objectively analyzed monthly fields (1955-2017), which include a large portion of the profiles included in UDASH. MIMOC (Schmidtko et al., 2013) is a monthly, isopycnal ocean climatology containing data from ITPs and data archived in the World Ocean Database. MIMOC preserves the surface mixed layer, minimizing both diapycnal and isopycnal smoothing of temperature and salinity. For more recent observations, we have included the World Ocean Atlas 2023 ”1991-2020 climate normals”, a recent objectively analyzed climatology from the World Ocean Atlas only covering the 1991-2020 period (WOA23, Boyer et al. (2018)).

ASTE (Arctic Subpolar gyre sTate Estimate, Nguyen et al. (2021) is a data-constrained ocean-sea ice model-data synthesis covering the period 2002-2017. The model (Massachusetts Institute of Technology general circulation model, MITgcm) uses various in-situ and satellite observations, including ITPs and moorings in the Arctic gateways. ECCOv4-r3 (Forget et al., 2015) is a global state estimate of ocean circulation and sea ice covering the period 1992 to 2015. It is also based on MITgcm, and assimilates various satellite and in-situ ocean observations. ECCOv4-r3 has demonstrated its ability to accurately reproduce ocean properties and variability in sub-Arctic regions (Asbjørnsen et al., 2020). For further details on the temporal and spatial data coverage, processing and data assimilation methods, data quality, and uncertainty estimates of the different climatologies and state estimates, we refer to the respective reference papers.

Data accessibility statement

All datasets used in this study are publicly available, in compliance with the MOSAiC data policy. In addition, we published a daily average dataset based on the 2434 temperature and salinity profiles, as outlined in the Appendix, and derived parameters, as listed in Tab. 4 in netCDF format (Schulz et al., 2023b), and created webODV compliant data files and views (Mieruch, 2023). We strongly advise that future studies using the data presented here also cite the respective original datasets listed below.

CO1 GPS buoy: Nicolaus et al. (2021); CTD Polarstern: Tippenhauer et al. (in reviewb,i); Ocean City CTD: Tippenhauer et al. (in reviewa,i); MSS: Schulz et al. (2023c); ITPs (including CDOM data): Toole and Krishfield (2016); PG buoy O4: Hoppmann et al. (2022b); thermosalinograph: Rex et al. (2021a); Haas et al. (2021); Kanzow et al. (2021); Rex et al. (2021b,c); ADCP: Baumann et al. (2021).

Author Contributions

Contributed to conception and design: KS, ZK, CJMH, EC, MM, IF, CH, MAG.

Contributed to acquisition of data: KS, ZK, MM, DB, CJMH, ESD, MH, EC, GL, TS, IF, CH, SK, TB, ST, MAG.

Contributed to analysis and interpretation of data: KS, ZK, MM, DB, CJMH, ESD, EC, GL, TS, AQ, IF, CH, SK, MV, MAG.

Drafted and/or revised this article: All authors.

Approved the submitted version for publication: All authors.

Acknowledgements

Data used in this manuscript were produced as part of the international Multidisciplinary drifting Observatory for the Study of the Arctic Climate (MOSAiC) project with the tag MOSAiC20192020 and the Project_ID: AWI_PS122_00. The Ice-Tethered Profiler data were collected and made available by the Ice-Tethered Profiler Program (Toole et al., 2011; Krishfield et al., 2008) based at the Woods Hole Oceanographic Institution (https://www2.whoi.edu/site/itp/). We thank all persons involved in the expedition of the Research Vessel *Polarstern* (Knust,

2017) during MOSAiC in 2019-2020 as listed in the MOSAiC extended acknowledgment Nixdorf et al. (2021). We especially thank everyone involved in the discussion during the Second MOSAiC Science Conference in Boulder, Colorado, which motivated this study. We would also like to thank Daniela Ransby (Pangaea) and Christopher Kracha (Arctic Data Center) for their great support with the data publications.

Funding

Financial support for KS was available through the German (BMBF) and UK (NERC) funded PEANUTS-project (grant number 03F0804A), and the NSF funded projects NSF-AccelNet-2020387 and OPP-1936506. ZK, TB and IF received funding through the AROMA (Arctic Ocean mixing processes and vertical fluxes of energy and matter) project by the Research Council of Norway (grant no 294396). MM and MAG were supported by funding from the European Union's Horizon 2020 research and innovation programme under grant agreement No 101003826 via project CRiceS (Climate Relevant interactions and feedbacks: the key role of sea ice and Snow in the polar and global climate system) and the Research Council of Norway through project HAVOC (grant no 280292). MV was supported through the Changing Arctic Ocean (CAO) program, jointly funded by the UKRI Natural Environment Research Council (NERC) and the BMBF, project Advective Pathways of nutrients and key Ecological substances in the ARctic (APEAR) grants NE/R012865/1, NE/R012865/2 and #03V01461. SK and CH were supported by the Swedish Research Council (grant 2018-03859 awarded to CH); participation of SK to MOSAiC was supported by the Swedish Research Polar Secretariat. ESD was supported by the European Union's Horizon 2020 research and innovation programme under grant agreement no. 821001; participation of ESD on MOSAiC was supported by the Natural Environment Research Council (NERC) through the EnvEast Doctoral Training Partnership (grant no. NE/L002582/1) and the UK Department for Business, Energy and Industrial Strategy (BEIS) through the UK Arctic Office. TS and the AOFB measurements are funded by NSF OPP-1723400. GL also gratefully acknowledges financial support from the Ocean Frontier Institute under a Canada First Research Excellence Fund award.

Competing interests

All authors declare that they have no competing interests.

References

Arrigo, KR, van Dijken, GL. 2015. Continued increases in Arctic Ocean primary production. *Progress in Oceanography* **136**: 60–70. doi:https://doi.org/10.1016/j.pocean.2015.05.002.

Asbjørnsen, H, Årthun, M, Skagseth, Ø, Eldevik, T. 2020. Mechanisms Underlying Recent Arctic Atlantification. *Geophysical Research Letters* **47**(15): e2020GL088036. ISSN 0094-8276. doi:https://doi.org/10.1029/2020GL088036.

Baker, MA, Gibson, CH. 1987. Sampling turbulence in the stratified ocean: Statistical consequences of strong intermittency. *Journal of Physical Oceanography* **17**(10): 1817–1836. doi:https://doi.org/10.1175/1520-0485(1987)017⟨1817:STITSO⟩2.0.CO;2.

Bates, N, Mathis, J. 2009. The Arctic Ocean marine carbon cycle: evaluation of air-sea CO 2 exchanges, ocean acidification impacts and potential feedbacks. *Biogeosciences* **6**(11): 2433–2459. doi:https://doi.org/10.5194/bg-6-2433-2009.

Bates, NR, Moran, SB, Hansell, DA, Mathis, JT. 2006. An increasing CO2 sink in the Arctic Ocean due to sea-ice loss. *Geophysical Research Letters* **33**(23). doi:https://doi.org/10.1029/2006GL027028.

Bauch, D, Cherniavskaia, E, Timokhov, L. 2016. Shelf basin exchange along the Siberian continental margin: Modification of Atlantic Water and Lower Halocline Water. *Deep Sea Research Part I: Oceanographic Research Papers* **115**: 188–198. doi:10.1016/j.dsr.2016.06.008.

Bauch, D, van der Loeff, MR, Andersen, N, Torres-Valdes, S, Bakker, K, Abrahamsen, EP. 2011. Origin of freshwater and polynya water in the Arctic Ocean halocline in summer 2007. *Progress in Oceanography* **91**(4): 482–495. doi:https://doi.org/10.1016/j.pocean.2011.07.017.

Baumann, T, Fer, I, Bryhni, H, Peterson, AK, Allerholt, J, Fang, YC, Hoppmann, M, Karam, S, Koenig, Z, Kong, B, Mohrholz, V, Muilwijk, M, Schaffer, J, Schulz, K, Sukhikh, N, Tippenhauer, S. 2021. Under-ice current measurements during MOSAiC from a 75 kHz acoustic Doppler profiler. PANGAEA. doi:https://doi.org/10.1594/PANGAEA.934792.

Behrendt, A, Sumata, H, Rabe, B, Schauer, U. 2018. UDASH - Unified Database for Arctic and Subarctic Hydrography. *Earth System Science Data* **10**(2): 1119–1138. ISSN 18663516. doi:https://doi.org/10.5194/essd-10-1119-2018.

Bouffard, D, Boegman, L. 2013. A diapycnal diffusivity model for stratified environmental flows. *Dynamics of Atmospheres and Oceans* **61**: 14–34. doi: https://doi.org/10.1016/j.dynatmoce.2013.02.002.

Bourgain, P, Gascard, JC. 2011. The Arctic Ocean halocline and its interannual variability from 1997 to 2008. *Deep Sea Research Part I: Oceanographic Research Papers* **58**(7): 745–756. doi:https://doi.org/10.1016/j.dsr.2011.05.001.

Boyd, TJ, Steele, M, Muench, RD, Gunn, JT. 2002. Partial recovery of the Arctic Ocean halocline. *Geophysical Research Letters* **29**(14): 2–1. doi:https://doi.org/10.1029/2001GL014047.

Boyer, TP, Antonov, JI, Baranova, OK, Coleman, C, Garcia, HE, Grodsky, A, Johnson, DR, Locarnini, Ra, Mishonov, AV, O'Brien, TD, Paver, CR, Reagan, JR, Seidov, D, Smolyar, IV, Zweng, MM, Brien, TDO, Paver, CR, Reagan, JR, Seidov, D, Smolyar, IV, Zweng, MM, Sullivan, KD. 2013. WORLD OCEAN DATABASE 2013, NOAA Atlas NESDIS 72. *Sydney Levitus, Ed; Alexey Mishonoc, Technical Ed* **NOAA Atlas**: 209 pp. doi: https://doi.org/10.7289/V5NZ85MT.

Boyer, TP, Garcia, HE, Locarnini, RA, Zweng, MM, Mishonov, AV, Reagan, JR, Weathers, KA, Baranova, OK, Seidov, D, Smolyar, IV. 2018. World Ocean Atlas 2018. *NOAA National Centers for Environmental Information* `https://www.ncei.noaa.gov/archive/accession/NCEI-WOA18`.

Carranza, MM, Gille, ST, Franks, PJ, Johnson, KS, Pinkel, R, Girton, JB. 2018. When mixed layers are not mixed. Storm-driven mixing and bio-optical vertical gradients in mixed layers of the Southern Ocean. *Journal of Geophysical Research: Oceans* **123**(10): 7264–7289. doi:https://doi.org/10.1029/2018JC014416.

Carter-Gates, M, Balestreri, C, Thorpe, SE, Cottier, F, Baylay, A, Bibby, TS, Moore, CM, Schroeder, DC. 2020. Implications of increasing Atlantic influence for Arctic microbial community structure. *Scientific reports* **10**(1): 19262. doi:https://doi.org/10.1038/s41598-020-76293-x.

Chamberlain, EJ, Sebastian Rottika, BR, D'Angelo, A, Creamean, J, Loose, B, Ulfsbo, A, Fong, AA, Hoppe, CJM, Droste, E, Nomura, D, Bowman, J. in prep. Microbial predictors of net productivity in the central Arctic Ocean. *Frontiers in Microbiology* .

Charette, MA, Kipp, LE, Jensen, LT, Dabrowski, JS, Whitmore, LM, Fitzsimmons, JN, Williford, T, Ulfsbo, A, Jones, E, Bundy, RM, Vivancos, SM, Pahnke, K, John, SG, Xiang, Y, Hatta, M, Petrova, MV, Heimbürger-Boavida, L, Bauch, D, Newton, R, Pasqualini, A, Agather, AM, Amon, RMW, Anderson, RF, Andersson, PS, Benner, R, Bowman, KL, Edwards, RL, Gdaniec, S, Gerringa, LJA, González, AG, Granskog, M, Haley, B, Hammerschmidt, CR, Hansell, DA, Henderson, PB, Kadko, DC, Kaiser, K, Laan, P, Lam, PJ, Lamborg, CH, Levier, M, Li, X, Margolin, AR, Measures, C, Middag, R, Millero, FJ, Moore, WS, Paffrath, R, Planquette, H, Rabe, B, Reader, H, Rember, R, Rijkenberg, MJA, Roy-Barman, M, Rutgers van der Loeff, M, Saito, M, Schauer, U, Schlosser, P, Sherrell, RM, Shiller, AM, Slagter, H, Sonke, JE, Stedmon, C, Woosley, RJ, Valk, O, Ooijen, J, Zhang, R. 2020. The Transpolar Drift as a Source of Riverine and Shelf-Derived Trace Elements to the Central Arctic Ocean. *Journal of Geophysical Research: Oceans* **125**(5): e2019JC015920. ISSN 2169-9275. doi:https://doi.org/10.1029/2019JC015920.

Dosser, H, Chanona, M, Waterman, S, Shibley, N, Timmermans, ML. 2021. Changes in internal wave-driven mixing across the Arctic Ocean: Finescale estimates from an 18-year pan-Arctic record. *Geophysical Research Letters* **48**(8): e2020GL091747. doi:https://doi.org/10.1029/2020GL091747.

Droste, ES, Hoppema, M, González-Dávila, M, Santana-Casiano, JM, Queste, BY, Dall'Olmo, G, Venables, HJ, Rohardt, G, Ossebaar, S, Schuller, D, et al. 2022. The influence of tides on the marine carbonate chemistry of a coastal polynya in the south-eastern Weddell Sea. *Ocean Science* **18**(5): 1293–1320. doi:https://doi.org/10.5194/os-18-1293-2022.

Environmental Working Group, V. 1997. Joint US-Russian atlas of the Arctic Ocean for the winter period. *Natl Snow and Ice Data Cent* .

Erofeeva, S, Egbert, G. 2020. Arc5km2018: Arctic Ocean Inverse Tide Model on a 5 kilometer grid, 2018. Dataset. Arctic Data Center. doi:10.18739/A21R6N14K.

Eveleth, R, Timmermans, ML, Cassar, N. 2014. Physical and biological controls on oxygen saturation variability in the upper Arctic Ocean. *Journal of Geophysical Research: Oceans* **119**: 7420–7432. doi:10.1002/2014JC009816.

Fer, I. 2009. Weak vertical diffusion allows maintenance of cold halocline in the central Arctic. *Atmospheric and Oceanic Science Letters* **2**(3): 148–152. doi:https://doi.org/10.1080/16742834.2009.11446789.

Fer, I, Baumann, TM, Koenig, Z, Muilwijk, M, Tippenhauer, S. 2022. Upper-Ocean Turbulence Structure and Ocean-Ice Drag Coefficient Estimates Using an Ascending Microstructure Profiler During the MOSAiC Drift. *Journal of Geophysical Research: Oceans* **127**(9): e2022JC018751. doi:https://doi.org/10.1029/2022JC018751.

Fer, I, Müller, M, Peterson, A. 2015. Tidal forcing, energetics, and mixing near the Yermak Plateau. *Ocean Sci* **11**: 287–304. doi:https://doi.org/10.5194/

os-11-287-2015.

Fine, EC, Cole, ST. 2022. Decadal Observations of Internal Wave Energy, Shear, and Mixing in the Western Arctic Ocean. *Journal of Geophysical Research: Oceans* **127**(5): e2021JC018056. doi:https://doi.org/10.1029/2021JC018056.

Forget, G, Campin, JM, Heimbach, P, Hill, CN, Ponte, RM, Wunsch, C. 2015. ECCO version 4: An integrated framework for non-linear inverse modeling and global ocean state estimation. *Geoscientific Model Development* **8**(10): 3071–3104. ISSN 1991-9603. doi:https://doi.org/10.5194/gmd-8-3071-2015.

Fouest, VL, Babin, M, Tremblay, JÉ. 2013. The fate of riverine nutrients on Arctic shelves. *Biogeosciences* **10**(6): 3661–3677. doi:https://doi.org/10.5194/bg-10-3661-2013.

Fransson, A, Chierici, M, Skjelvan, I, Olsen, A, Assmy, P, Peterson, AK, Spreen, G, Ward, B. 2017. Effects of sea-ice and biogeochemical processes and storms on under-ice water fCO2 during the winter-spring transition in the high Arctic Ocean: Implications for sea-air CO2 fluxes. *Journal of Geophysical Research: Oceans* **122**(7): 5566–5587. doi:https://doi.org/10.1002/2016JC012478.

Friis, K, Körtzinger, A, Wallace, DW. 2003. The salinity normalization of marine inorganic carbon chemistry data. *Geophysical Research Letters* **30**(2). doi:https://doi.org/10.1029/2002GL015898.

Galand, PE, Potvin, M, Casamayor, EO, Lovejoy, C. 2010. Hydrography shapes bacterial biogeography of the deep Arctic Ocean. *The ISME journal* **4**(4): 564–576. doi:https://doi.org/10.1038/ismej.2009.134.

Gibson, GA, Elliot, S, Clement Kinney, J, Piliouras, A, Jeffery, N. 2022. Assessing the potential impact of river chemistry on arctic coastal production. *Frontiers in Marine Science* **9**: 738363. doi:https://doi.org/10.3389/fmars.2022.738363.

Gonçalves-Araujo, R, Granskog, MA, Bracher, A, Azetsu-Scott, K, Dodd, PA, Stedmon, CA. 2016. Using fluorescent dissolved organic matter to trace and distinguish the origin of Arctic surface waters. *Scientific Reports* **6**(1): 33978. ISSN 2045-2322. doi:https://doi.org/10.1038/srep33978.

Gonçalves-Araujo, R, Rabe, B, Peeken, I, Bracher, A. 2018. High colored dissolved organic matter (CDOM) absorption in surface waters of the central-eastern Arctic Ocean: Implications for biogeochemistry and ocean color algorithms. *PLOS ONE* **13**: e0190838. doi:10.1371/journal.pone.0190838.

Gordó-Vilaseca, C, Stephenson, F, Coll, M, Lavin, C, Costello, MJ. 2023. Three decades of increasing fish biodiversity across the northeast Atlantic and the Arctic Ocean. *Proceedings of the National Academy of Sciences* **120**(4): e2120869120. doi:https://doi.org/10.1073/pnas.2120869120.

Granskog, MA, Macdonald, RW, Mundy, CJ, Barber, DG. 2007. Distribution, characteristics and potential impacts of chromophoric dissolved organic matter (CDOM) in Hudson Strait and Hudson Bay, Canada. *Continental Shelf Research* **27**: 2032–2050. doi:https://doi.org/10.1016/j.csr.2007.05.001.

Granskog, MA, Pavlov, AK, Sagan, S, Kowalczuk, P, Raczkowska, A, Stedmon, CA. 2015. Effect of sea-ice melt on inherent optical properties and vertical distribution of solar radiant heating in Arctic surface waters. *Journal of Geophysical Research: Oceans* **120**(10): 7028–7039. ISSN 2169-9275. doi:10.1002/2015JC011087.

Guthrie, J, Fer, I, Morison, J. 2017. Thermohaline Staircases in the Amundsen Basin: possible disruption by shear and mixing. *Journal of Geophysical Research: Oceans* **122**: 7767– 7782. doi:https://doi.org/10.1002/2017JC012993.

Haas, C, Hoppmann, M, Tippenhauer, S, Rohardt, G. 2021. Continuous thermosalinograph oceanography along RV POLARSTERN cruise track PS122/2. PANGAEA. doi:https://doi.org/10.1594/PANGAEA.930024.

Han, D, Ha, HK, Hwang, CY, Lee, BY, Hur, HG, Lee, YK. 2015. Bacterial communities along stratified water columns at the Chukchi Borderland in the western Arctic Ocean. *Deep Sea Research Part II: Topical Studies in Oceanography* **120**: 52–60. doi:https://doi.org/10.1016/j.dsr2.2015.01.018.

Heuzé, C, Huhn, O, Walter, M, Sukhikh, N, Karam, S, Körtke, W, Vredenborg, M, Bulsiewicz, K, Sültenfuß, J, Fang, YC, Mertens, C, Rabe, B, Tippenhauer, S, Allerholt, J, He, H, Kuhlmey, D, Kuznetsov, I, Mallet, M. 2023a. A year of transient tracers chlorofluorocarbon 12 and sulfur hexafluoride, noble gases helium and neon, and tritium in the Arctic Ocean from the MOSAiC expedition (2019-2020). *Earth System Science Data Discussions* doi:10.5194/essd-2023-232.

Heuzé, C, Zanowski, H, Karam, S, Muilwijk, M. 2023b. The deep Arctic Ocean and Fram Strait in CMIP6 models. *Journal of Climate* **36**(8): 2551–2584. doi:https://doi.org/10.1175/JCLI-D-22-0194.1.

Hill, VJ. 2008. Impacts of chromophoric dissolved organic material on surface ocean heating in the Chukchi Sea. *Journal of Geophysical Research* **113**: C07024. doi:10.1029/2007JC004119.

Hoppmann, M, Kuznetsov, I, Fang, YC, Rabe, B. 2022a. Mesoscale observations of temperature and salinity in the Arctic Transpolar Drift: a high-resolution dataset from the MOSAiC Distributed Network. *Earth System Science Data* **14**(11): 4901–4921. doi:https://doi.org/10.5194/essd-14-4901-2022.

Hoppmann, M, Kuznetsov, I, Fang, YC, Rabe, B. 2022b. Processed data of CTD buoys 2019O1 to 2019O8 as part of the MOSAiC Distributed Network. PANGAEA. doi:https://doi.org/10.1594/PANGAEA.940320.

Jakobsson, M, Mayer, LA, Bringensparr, C, Castro, CF, Mohammad, R, Johnson, P, Ketter, T, Accettella, D, Amblas, D, An, L, et al. 2020. The international bathymetric chart of the Arctic Ocean version 4.0. *Scientific data* **7**(1): 176. doi:https://doi.org/10.1038/s41597-020-0520-9.

Janout, MA, Hölemann, J, Laukert, G, Smirnov, A, Krumpen, T, Bauch, D, Timokhov, L. 2020. On the variability of stratification in the freshwater-influenced Laptev Sea Region. *Frontiers in Marine Science* **7**: 543489. doi: https://doi.org/10.3389/fmars.2020.543489.

Juranek, LW. 2022. Changing biogeochemistry of the Arctic Ocean. *Oceanography* **35**(3/4): 144–155. doi:https://doi.org/10.5670/oceanog.2022.120.

Kanzow, T, Hoppmann, M, Tippenhauer, S, Rohardt, G. 2021. Continuous thermosalinograph oceanography along RV POLARSTERN cruise track PS122/3. PANGAEA. doi:https://doi.org/10.1594/PANGAEA.930026.

Karam, S, Heuzé, C, Müller, V, Zheng, Y. 2023. Recirculation of Canada Basin Deep Water in the Amundsen Basin, Arctic. *Journal of Physical Oceanography* **accepted**.

Karcher, M, Smith, JN, Kauker, F, Gerdes, R, Smethie, WM. 2012. Recent changes in Arctic Ocean circulation revealed by iodine-129 observations and modeling. *Journal of Geophysical Research* **117**: C08007. doi:10.1029/2011JC007513.

Kawaguchi, Y, Koenig, Z, Nomura, D, Hoppmann, M, Inoue, J, Fang, YC, Schulz, K, Gallagher, M, Katlein, C, Nicolaus, M, et al. 2022. Turbulent mixing during late summer in the ice–ocean boundary layer in the central Arctic Ocean: Results from the MOSAiC expedition. *Journal of Geophysical Research: Oceans* **127**(8): e2021JC017975. doi:https://doi.org/10.1029/2021JC017975.

Kim, YH, Min, SK, Gillett, NP, Notz, D, Malinina, E. 2023. Observationally-constrained projections of an ice-free Arctic even under a low emission scenario. *Nature Communications* **14**. doi:https://doi.org/10.1038/s41467-023-38511-8.

Knust, R. 2017. Polar research and supply vessel POLARSTERN operated by the Alfred-Wegener-Institute. *Journal of Large-Scale Research Facilities* **3**: A119. doi:https://doi.org/10.17815/jlsrf-3-163.

Kong, X. 2022. *Molecular and optical characterization of dissolved organic matter in the Central Arctic Ocean*. Phd thesis, University of Bremen, Dissertation, 2022, Bremen. 159 pages. https://suche.suub.uni-bremen.de/peid=B183177399.

Korhonen, M, Rudels, B, Marnela, M, Wisotzki, A, Zhao, J. 2013. Time and space variability of freshwater content, heat content and seasonal ice melt in the Arctic Ocean from 1991 to 2011. *Ocean Science* **9**(6): 1015–1055. doi:https://doi.org/10.5194/osd-9-2621-2012.

Krishfield, R, Toole, J, Proshutinsky, A, Timmermans, ML. 2008. Automated ice-tethered profilers for seawater observations under pack ice in all seasons. *Journal of Atmospheric and Oceanic Technology* **25**(11): 2091–2105. doi:https://doi.org/10.1175/2008JTECHO587.1.

Krumpen, T, Belter, HJ, Boetius, A, Damm, E, Haas, C, Hendricks, S, Nicolaus, M, Nöthig, EM, Paul, S, Peeken, I, et al. 2019. Arctic warming interrupts the Transpolar Drift and affects long-range transport of sea ice and ice-rafted matter. *Scientific Reports* **9**(1): 5459. doi:https://doi.org/10.1038/s41598-019-41456-y.

Kwok, R. 2018. Arctic sea ice thickness, volume, and multiyear ice coverage: losses and coupled variability (1958–2018). *Environmental Research Letters* **13**(10): 105005. doi:https://doi.org/10.1088/1748-9326/aae3ec.

Lannuzel, D, Tedesco, L, Van Leeuwe, M, Campbell, K, Flores, H, Delille, B, Miller, L, Stefels, J, Assmy, P, Bowman, J, et al. 2020. The future of Arctic sea-ice biogeochemistry and ice-associated ecosystems. *Nature Climate Change* **10**(11): 983–992. doi:https://doi.org/10.1038/s41558-020-00940-4.

Laukert, G, Bauch, D, Rabe, B, Damm, E, Krumpen, T, Kienast, SS, Kienast, M, Hathorne, E, Vredenborg, M, Tippenhauer, S, Simões Pereira, P, D'Angelo, A, Nomura, D. in prep. Decoupled sea ice and surface ocean pathways of Siberian river water along the Arctic Transpolar Drift. *Nature Communications* .

Laukert, G, Frank, M, Bauch, D, Hathorne, EC, Rabe, B, von Appen, WJ, Wegner, C, Zieringer, M, Kassens, H. 2017. Ocean circulation and freshwater pathways in the Arctic Mediterranean based on a combined Nd isotope, REE and oxygen isotope section across Fram Strait. *Geochimica et Cosmochimica Acta* **202**: 285–309. doi:https://doi.org/10.1016/j.gca.2016.12.028.

Laukert, G, Grasse, P, Novikhin, A, Povazhnyi, V, Doering, K, Hölemann, J, Janout, M, Bauch, D, Kassens, H, Frank, M. 2022. Nutrient and silicon isotope dynamics in the Laptev Sea and implications for nutrient availability in the transpolar drift. *Global Biogeochemical Cycles* **36**(9): e2022GB007316.

doi:https://doi.org/10.1029/2022GB007316.

Laukert, G, Makhotin, M, Petrova, MV, Frank, M, Hathorne, EC, Bauch, D, Böning, P, Kassens, H. 2019. Water mass transformation in the Barents Sea inferred from radiogenic neodymium isotopes, rare earth elements and stable oxygen isotopes. *Chemical Geology* **511**: 416–430. doi:https://doi.org/10.1016/j.chemgeo.2018.10.002.

Lei, R, Cheng, B, Hoppmann, M, Zhang, F, Zuo, G, Hutchings, JK, Lin, L, Lan, M, Wang, H, Regnery, J, et al. 2022. Seasonality and timing of sea ice mass balance and heat fluxes in the Arctic transpolar drift during 2019–2020. *Elementa Science of the Anthropocene* **10**(1): 000089. doi:https://doi.org/10.1525/elementa.2021.000089.

Lenn, YD, Wiles, P, Torres-Valdes, S, Abrahamsen, E, Rippeth, T, Simpson, J, Bacon, S, Laxon, S, Polyakov, I, Ivanov, V, et al. 2009. Vertical mixing at intermediate depths in the Arctic boundary current. *Geophysical Research Letters* **36**(5). doi:https://doi.org/10.1029/2008GL036792.

Li, WK, McLaughlin, FA, Lovejoy, C, Carmack, EC. 2009. Smallest algae thrive as the Arctic Ocean freshens. *Science* **326**(5952): 539–539. doi:10.1126/science.1179798.

Llanillo, P, Aiken, CM, Cordero, R, Damiani, A, Sepúlveda, E, Fernández-Gómez, B. 2019. Oceanographic variability induced by tides, the intraseasonal cycle and warm subsurface water intrusions in Maxwell Bay, King George Island (West-Antarctica). *Scientific reports* **9**(1): 18571. doi:https://doi.org/10.1038/s41598-019-54875-8.

Locarnini, R, Mishonov, A, Baranova, O, Boyer, T, Zweng, M, Garcia, H, Reagan, J, Seidov, D, Weathers, K, Paver, C, Smolyar, I. 2018. *World Ocean Atlas 2018, Volume 1: Temperature*. A. Mishonov Technical Ed.; NOAA Atlas NESDIS 81.

Marnela, M, Rudels, B, Goszczko, I, Beszczynska-Möller, A, Schauer, U. 2016. Fram Strait and Greenland Sea transports, water masses, and water mass transformations 1999–2010 (and beyond). *Journal of Geophysical Research: Oceans* **121**(4): 2314–2346. doi:https://doi.org/10.1002/2015JC011312.

McDougall, TJ, Barker, PM. 2011. Getting started with TEOS-10 and the Gibbs Seawater (GSW) oceanographic toolbox. *SCOR/IAPSO WG* **127**: 1–28.

McPhee, M. 2008. *Air-ice-ocean interaction: Turbulent ocean boundary layer exchange processes*. Springer Science & Business Media.

Meyer, A, Fer, I, Sundfjord, A, Peterson, AK. 2017a. Mixing rates and vertical heat fluxes north of Svalbard from Arctic winter to spring. *Journal of Geophysical Research: Oceans* **122**(6): 4569–4586. doi:https://doi.org/10.1002/

2016JC012441.

Meyer, A, Sundfjord, A, Fer, I, Provost, C, Villacieros Robineau, N, Koenig, Z, Onarheim, IH, Smedsrud, LH, Duarte, P, Dodd, PA, et al. 2017b. Winter to summer oceanographic observations in the Arctic Ocean north of Svalbard. *Journal of Geophysical Research: Oceans* **122**(8): 6218–6237. doi:https://doi.org/10.1002/2016JC012391.

Mieruch, S. 2023. smieruch/mosaic_hydrographic_core_parameters: Initial Release. Zenodo. doi:10.5281/zenodo.8304184. https://doi.org/10.5281/zenodo.8304184.

Mieruch, S, Schlitzer, R. 2023. smieruch/webodv: webODV v1.0.0. Zenodo. doi:10.5281/zenodo.8241241. https://doi.org/10.5281/zenodo.8241241.

Morán, XAG, López-Urrutia, Á, Calvo-Díaz, A, Li, WK. 2010. Increasing importance of small phytoplankton in a warmer ocean. *Global Change Biology* **16**(3): 1137–1144. doi:https://doi.org/10.1111/j.1365-2486.2009.01960.x.

Mysak, LA. 2001. Patterns of Arctic Circulation. *Science* **293**(5533): 1269–1270. doi:DOI:10.1126/science.1064217.

Nansen, F. 1902. Oceanography of the North Polar basin. The Norwegian North Polar Expedition 1893–1896. Scientific results 9 (3): 427. Greenwood Press, New York.

Nguyen, AT, Pillar, H, Ocaña, V, Bigdeli, A, Smith, TA, Heimbach, P. 2021. The Arctic Subpolar Gyre sTate Estimate: Description and Assessment of a Data-Constrained, Dynamically Consistent Ocean-Sea Ice Estimate for 2002–2017. *Journal of Advances in Modeling Earth Systems* **13**(5): e2020MS002398. doi:https://doi.org/10.1029/2020MS002398.

Nicolaus, M, Perovich, DK, Spreen, G, Granskog, MA, von Albedyll, L, Angelopoulos, M, Anhaus, P, Arndt, S, Belter, HJ, Bessonov, V, et al. 2022. Overview of the MOSAiC expedition: Snow and sea ice. *Elem Sci Anth* **10**(1): 000046. doi:https://doi.org/10.1525/elementa.2021.000046.

Nicolaus, M, Riemann-Campe, K, Bliss, A, Hutchings, JK, Granskog, MA, Haas, C, Hoppmann, M, Kanzow, T, Krishfield, RA, Lei, R, Rex, M, Li, T, Rabe, B. 2021. Drift trajectories of the main sites of the Distributed Network of MOSAiC 2019/2020. PANGAEA. doi:https://doi.org/10.1594/PANGAEA.937204.

Nixdorf, U, Dethloff, K, Rex, M, Shupe, M, Sommerfeld, A, Perovich, DK, Nicolaus, M, Heuzé, C, Rabe, B, Loose, B, Damm, E, Gradinger, R, Fong, A, Maslowski, W, Rinke, A, Kwok, R, Spreen, G, Wendisch, M, Herber, A, Hirsekorn, M, Mohaupt, V, Frickenhaus, S, Immerz, A, Weiss-Tuider, K, König, B, Mengedoht, D, Regnery, J, Gerchow, P, Ransby, D, Krumpen, T, Morgenstern, A, Haas, C, Kanzow, T, Rack, FR, Saitzev, V, Sokolov, V, Makarov, A, Schwarze, S, Wunderlich, T, Wurr, K, Boetius, A. 2021. MOSAiC Extended Acknowledgement. Zenodo. doi:https://doi.org/10.5281/zenodo.5541624.

Nomura, D, Kawaguchi, Y, Webb, AL, Li, Y, Dall'osto, M, Schmidt, K, Droste, ES, Chamberlain, EJ, Kolabutin, N, Shimanchuk, E, et al. 2023. Meltwater layer dynamics in a central Arctic lead: Effects of lead width, re-freezing, and mixing during late summer. *Elementa: Science of the Anthropocene* **11**(1). doi:https://doi.org/10.1525/elementa.2022.00102.

Östlund, HG, Hut, G. 1984. Arctic Ocean water mass balance from isotope data. *Journal of Geophysical Research: Oceans* **89**(C4): 6373–6381. doi:https://doi.org/10.1029/JC089iC04p06373.

Paffrath, R, Laukert, G, Bauch, D, Rutgers van der Loeff, M, Pahnke, K. 2021. Separating individual contributions of major Siberian rivers in the Transpolar Drift of the Arctic Ocean. *Scientific Reports* **11**(1): 1–11. doi:https://doi.org/10.1038/s41598-021-86948-y.

Pavlov, AK, Granskog, MA, Stedmon, CA, Ivanov, BV, Hudson, SR, Falk-Petersen, S. 2015. Contrasting optical properties of surface waters across the Fram Strait and its potential biological implications. *Journal of Marine Systems* **143**: 62–72. ISSN 09247963. doi:10.1016/j.jmarsys.2014.11.001.

Peralta-Ferriz, C, Woodgate, RA. 2015. Seasonal and interannual variability of pan-Arctic surface mixed layer properties from 1979 to 2012 from hydrographic data, and the dominance of stratification for multiyear mixed layer depth shoaling. *Progress in Oceanography* **134**: 19–53. doi:https://doi.org/10.1016/j.pocean.2014.12.005.

Perovich, D, Raphael, I, Moore, R, Clemens–Sewall, D, Lei, R, Sledd, A, Polashenski, C. under review. Sea ice heat and mass balance measurements from four autonomous buoys during the MOSAiC drift campaign. *Elementa: Science of the Anthropocene* .

Polyakov, IV, Pnyushkov, AV, Alkire, MB, Ashik, IM, Baumann, TM, Carmack, EC, Goszczko, I, Guthrie, J, Ivanov, VV, Kanzow, T, et al. 2017. Greater role for Atlantic inflows on sea-ice loss in the Eurasian Basin of the Arctic Ocean. *Science* **356**(6335): 285–291. doi:https://doi.org/10.1126/science.aai8204.

Polyakov, IV, Rippeth, TP, Fer, I, Alkire, MB, Baumann, TM, Carmack, EC, Ingvaldsen, R, Ivanov, VV, Janout, M, Lind, S, et al. 2020a. Weakening of cold halocline layer exposes sea ice to oceanic heat in the eastern Arctic Ocean. *Journal of Climate* **33**(18): 8107–8123. doi:https://doi.org/10.1175/

JCLI-D-19-0976.1.

Polyakov, IV, Rippeth, TP, Fer, I, Baumann, TM, Carmack, EC, Ivanov, VV, Janout, M, Padman, L, Pnyushkov, AV, Rember, R. 2020b. Intensification of near-surface currents and shear in the Eastern Arctic Ocean. *Geophysical Research Letters* **47**(16): e2020GL089469. doi:https://doi.org/10.1029/2020GL089469.

Priest, T, von Appen, WJ, Oldenburg, E, Popa, O, Torres-Valdés, S, Bienhold, C, Metfies, K, Boulton, W, Mock, T, Fuchs, BM, et al. 2023. Atlantic water influx and sea-ice cover drive taxonomic and functional shifts in Arctic marine bacterial communities. *The ISME Journal* pp. 1–14. doi:https://doi.org/10.1038/s41396-023-01461-6.

Rabe, B, Heuzé, C, Regnery, J, Aksenov, Y, Allerholt, J, Athanase, M, Bai, Y, Basque, C, Bauch, D, Baumann, TM, Chen, D, Cole, ST, Craw, L, Davies, A, Damm, E, Dethloff, K, Divine, DV, Doglioni, F, Ebert, F, Fang, YC, Fer, I, Fong, AA, Gradinger, R, Granskog, MA, Graupner, R, Haas, C, He, H, He, Y, Hoppmann, M, Janout, M, Kadko, D, Kanzow, T, Karam, S, Kawaguchi, Y, Koenig, Z, Kong, B, Krishfield, RA, Krumpen, T, Kuhlmey, D, Kuznetsov, I, Lan, M, Lei, R, Li, T, Torres-Valdés, S, Lin, L, Lin, L, Liu, H, Liu, N, Loose, B, Ma, X, MacKay, R, Mallet, M, Mallett, RDC, Maslowski, W, Mertens, C, Mohrholz, V, Muilwijk, M, Nicolaus, M, O'Brien, JK, Perovich, D, Ren, J, Rex, M, Ribeiro, N, Rinke, A, Schaffer, J, Schuffenhauer, I, Schulz, K, Shupe, MD, Shaw, W, Sokolov, V, Sommerfeld, A, Spreen, G, Stanton, T, Stephens, M, Su, J, Sukhikh, N, Sundfjord, A, Thomisch, K, Tippenhauer, S, Toole, JM, Vredenborg, M, Walter, M, Wang, H, Wang, L, Wang, Y, Wendisch, M, Zhao, J, Zhou, M, Zhu, J, Laukert, G. 2022. Overview of the MOSAiC expedition: Physical oceanography. *Elementa: Science of the Anthropocene* **10**(1). doi:https://doi.org/10.1525/elementa.2021.00062.

Randelhoff, A, Holding, J, Janout, M, Sejr, MK, Babin, M, Tremblay, JE, Alkire, MB. 2020. Pan-Arctic Ocean Primary Production Constrained by Turbulent Nitrate Fluxes. *Frontiers in Marine Science* **7**: 150. doi:https://doi.org/10.3389/fmars.2020.00150.

Rantanen, M, Karpechko, AY, Lipponen, A, Nordling, K, Hyvärinen, O, Ruosteenoja, K, Vihma, T, Laaksonen, A. 2022. The Arctic has warmed nearly four times faster than the globe since 1979. *Communications Earth & Environment* **3**(1): 168. doi:https://doi.org/10.1038/s43247-022-00498-3.

Rex, M, Hoppmann, M, Tippenhauer, S, Rohardt, G. 2021a. Continuous thermosalinograph oceanography along RV POLARSTERN cruise track PS122/1. PANGAEA. doi:https://doi.org/10.1594/PANGAEA.930023.

Rex, M, Hoppmann, M, Tippenhauer, S, Rohardt, G. 2021b. Continuous thermosalinograph oceanography along RV POLARSTERN cruise track PS122/4. PANGAEA. doi:https://doi.org/10.1594/PANGAEA.930027.

Rex, M, Hoppmann, M, Tippenhauer, S, Rohardt, G. 2021c. Continuous thermosalinograph oceanography along RV POLARSTERN cruise track PS122/5. PANGAEA. doi:https://doi.org/10.1594/PANGAEA.930028.

Rippeth, TP, Lincoln, BJ, Lenn, YD, Green, JM, Sundfjord, A, Bacon, S. 2015. Tide-mediated warming of Arctic halocline by Atlantic heat fluxes over rough topography. *Nature Geoscience* **8**(3): 191. doi:https://doi.org/10.1038/ngeo2350.

Rogge, A, Janout, M, Loginova, N, Trudnowska, E, Hörstmann, C, Wekerle, C, Oziel, L, Schourup-Kristensen, V, Ruiz-Castillo, E, Schulz, K, et al. 2023. Carbon dioxide sink in the Arctic Ocean from cross-shelf transport of dense Barents Sea water. *Nature Geoscience* **16**(1): 82–88. doi:https://doi.org/10.1038/s41561-022-01069-z.

Rudels, B. 2009. Arctic ocean circulation. Academic Press.

Rudels, B. 2015. Arctic Ocean circulation, processes and water masses: A description of observations and ideas with focus on the period prior to the International Polar Year 2007–2009. *Progress in Oceanography* **132**: 22–67. doi:https://doi.org/10.1016/j.pocean.2013.11.006.

Rudels, B, Hainbucher, D. 2020. On the formation and spreading of thermohaline intrusions in the Arctic Ocean. *Geophysica* **55**(1-2): 23–59.

Rudels, B, et al. 2012. Arctic Ocean circulation and variability-advection and external forcing encounter constraints and local processes. *Ocean Science* doi: https://doi.org/10.5194/os-8-261-2012.

Salganik, E, Katlein, C, Lange, BA, Matero, I, Lei, R, Fong, AA, Fons, SW, Divine, D, Oggier, M, Castellani, G, et al. 2023a. Temporal evolution of under-ice meltwater layers and false bottoms and their impact on summer Arctic sea ice mass balance. *Elementa: Science of the Anthropocene* **11**(1). doi:https://doi.org/10.1525/elementa.2022.00035.

Salganik, E, Lange, BA, Katlein, C, Matero, I, Anhaus, P, Høyland, KV, Granskog, MA. 2023b. Observations of preferential summer melt of Arctic sea-ice ridge keels from repeated multibeam sonar surveys. *The Cryosphere Discussions* doi:10.5194/tc-2023-106.

Schauer, U, Muench, RD, Rudels, B, Timokhov, L. 1997. Impact of eastern Arctic shelf waters on the Nansen Basin intermediate layers. *Journal of Geophysical Research: Oceans* **102**(C2): 3371–3382. doi:https://doi.org/10.1029/96JC03366.

Schmale, J, Zieger, P, Ekman, AM. 2021. Aerosols in current and future Arctic climate. *Nature Climate Change* **11**(2): 95–105. doi:https://doi.org/10.1038/s41558-020-00969-5.

Schmidtko, S, Johnson, GC, Lyman, JM. 2013. MIMOC: A global monthly isopycnal upper-ocean climatology with mixed layers. *Journal of Geophysical Research: Oceans* **118**(4). ISSN 21699291. doi:https://doi.org/10.1002/jgrc.20122.

Schulz, K, Janout, M, Lenn, YD, Ruiz-Castillo, E, Polyakov, I, Mohrholz, V, Tippenhauer, S, Reeve, K, Hölemann, J, Rabe, B, Vredenborg, M. 2021. On the along-slope heat loss of the Boundary Current in the Eastern Arctic Ocean. *Journal of Geophysical Research: Oceans* **126**(2): e2020JC016375. doi:https://doi.org/10.1029/2020JC016375.

Schulz, K, Kadko, D, Mohrholz, V, Stephens, M, Fer, I. 2023a. Winter vertical diffusion rates in the Arctic Ocean, estimated from 7Be measurements and dissipation rate profiles. *Journal of Geophysical Research: Oceans* pp. e2022JC019197. doi:https://doi.org/10.1029/2022JC019197.

Schulz, K, Koenig, Z, Muilwijk, M. 2023b. The Eurasian Arctic Ocean along the MOSAiC drift (2019-2020): Core hydrographic parameters. Arctic Data Center. doi:doi:10.18739/A21J9790B.

Schulz, K, Lincoln, B, Povazhnyy, V, Rippeth, T, Lenn, YD, Janout, M, Alkire, M, Scannell, B, Torres-Valdés, S. 2022a. Increasing nutrient fluxes and mixing regime changes in the eastern Arctic Ocean. *Geophysical Research Letters* pp. e2021GL096152. doi:https://doi.org/10.1029/2021GL096152.

Schulz, K, Mohrholz, V, Fer, I, Janout, M, Hoppmann, M, Schaffer, J, Koenig, Z. 2022b. A full year of turbulence measurements from a drift campaign in the Arctic Ocean 2019—2020. *Scientific Data* **9**(472). doi:https://doi.org/10.1038/s41597-022-01574-1.

Schulz, K, Mohrholz, V, Fer, I, Janout, MA, Hoppmann, M, Schaffer, J, Koenig, Z, Rabe, B, Heuzé, C, Regnery, J, Allerholt, J, Fang, YC, He, H, Kanzow, T, Karam, S, Kuznetsov, I, Kong, B, Liu, H, Muilwijk, M, Schuffenhauer, I, Sukhikh, N, Sundfjord, A, Tippenhauer, S. 2023c. Turbulent microstructure profile (MSS) measurements from the MOSAiC drift, Arctic Ocean, version 2. PANGAEA. doi:https://doi.pangaea.de/10.1594/PANGAEA.961798.

Schuster, U, McKinley, GA, Bates, N, Chevallier, F, Doney, SC, Fay, AR, González-Dávila, M, Gruber, N, Jones, S, Krijnen, J, et al. 2013. An assessment of the Atlantic and Arctic sea–air CO 2 fluxes, 1990–2009. *Biogeosciences* **10**(1): 607–627. doi:https://doi.org/10.5194/bg-10-607-2013.

Shaw, WJ, Stanton, TP. 2014. Vertical diffusivity of the Western Arctic Ocean halocline. *Journal of Geophysical Research: Oceans* **119**(8): 5017–5038. doi:https://doi.org/10.1002/2013JC009598.

Shibley, NC, Timmermans, ML, Carpenter, JR, Toole, JM. 2017. Spatial variability of the Arctic Ocean's double-diffusive staircase. *Journal of Geophysical Research: Oceans* **122**(2): 980–994. doi:https://doi.org/10.1002/2016JC012419.

Shupe, MD, Rex, M, Blomquist, B, Persson, POG, Schmale, J, Uttal, T, Althausen, D, Angot, H, Archer, S, Bariteau, L, et al. 2022. Overview of the MOSAiC expedition: Atmosphere. University of California Press. doi:https://doi.org/10.1525/elementa.2021.00060.

Sirevaag, A, Fer, I. 2012. Vertical heat transfer in the Arctic Ocean: The role of double-diffusive mixing. *Journal of Geophysical Research: Oceans* **117**(C7). doi:https://doi.org/10.1029/2012JC007910.

Skogseth, R, McPhee, MG, Nilsen, F, Smedsrud, LH. 2013. Creation and tidal advection of a cold salinity front in Storfjorden: 1. Polynya dynamics. *Journal of Geophysical Research: Oceans* **118**(7): 3278–3291. doi:https://doi.org/10.1002/jgrc.20231.

Smedsrud, LH, Esau, I, Ingvaldsen, RB, Eldevik, T, Haugan, PM, Li, C, Lien, VS, Olsen, A, Omar, AM, Otterå, OH, et al. 2013. The role of the Barents Sea in the Arctic climate system. *Reviews of Geophysics* **51**(3): 415–449. doi:https://doi.org/10.1002/rog.20017.

Smethie Jr, W, Chipman, D, Swift, J, Koltermann, K. 1988. Chlorofluoromethanes in the Arctic Mediterranean seas: evidence for formation of bottom water in the Eurasian Basin and deep-water exchange through Fram Strait. *Deep Sea Research Part A Oceanographic Research Papers* **35**(3): 347–369. doi:https://doi.org/10.1016/0198-0149(88)90015-5.

Smith, MM, Angot, H, Chamberlain, EJ, Droste, ES, Karam, S, Muilwijk, M, Webb, AL, Archer, SD, Beck, I, Blomquist, BW, Bowman, J, Boyer, M, Bozzato, D, Chierici, M, Creamean, J, D'Angelo, A, Delille, B, Fer, I, Fong, AA, Fransson, A, Fuchs, N, Gardner, J, Granskog, MA, Hoppe, CJM, Hoppema, M, Hoppmann, M, Mock, T, Muller, S, Müller, O, Nicolaus, M, Nomura, D, Petäjä, T, Salganik, E, Schmale, J, Schmidt, K, Schulz, K, Shupe, MD, Stefels, J, Thielke, L, Tippenhauer, S, Ulfsbo, A, van Leeuwe, M, Webster, M, Yoshimura, M, Zhan, L. 2023. Thin and transient meltwater layers and false bottoms in the Arctic sea ice pack – recent insights on these historically overlooked features. *Elementa: Science of the Anthropocene (accepted)* .

Smith, MM, von Albedyll, L, Raphael, IA, Lange, BA, Matero, I, Salganik, E, Webster, MA, Granskog, MA, Fong, A, Lei, R, Light, B. 2022. Quantifying false bottoms and under-ice meltwater layers beneath Arctic summer sea ice with fine-scale observations. *Elementa: Science of the Anthropocene* **10**(1): 000116. ISSN 2325-1026. doi:10.1525/elementa.2021.000116.

Snoeijs-Leijonmalm, P, Flores, H, Sakinan, S, Hildebrandt, N, Svenson, A, Castellani, G, Vane, K, Mark, FC, Heuzé, C, Tippenhauer, S, et al. 2022. Unexpected fish and squid in the central Arctic deep scattering layer. *Science advances* **8**(7): eabj7536. doi:https://doi.org/10.1126/sciadv.abj7536.

Somavilla, R, Schauer, U, Budéus, G. 2013. Increasing amount of Arctic Ocean deep waters in the Greenland Sea. *Geophysical Research Letters* **40**(16): 4361–4366. doi:https://doi.org/10.1002/grl.50775.

Son, E, Kawaguchi, Y, Cole, S, Toole, J, Ha, H. 2022. Assessment of Turbulent Mixing Associated With Eddy-Wave Coupling Based on Autonomous Observations From the Arctic Canada Basin. *Journal of Geophysical Research: Oceans* **127**(9): e2022JC018489. doi:https://doi.org/10.1029/2022JC018489.

Stanton, T, Shaw, W, Perovich, D. in prep. Controls of ice-ocean scalar fluxes during the MOSAiC Transpolar drift. .

Stedmon, CA, Amon, RMW, Bauch, D, Bracher, A, Gonçalves-Araujo, R, Hoppmann, M, Krishfield, RA, Laney, S, Rabe, B, Reader, HE, Granskog, MA. 2021. Intercalibrated dataset of in situ dissolved organic matter fluorescence collected using Ice Tethered Profilers in the Central Arctic (2011-2016). PANGAEA. doi:10.1594/PANGAEA.934370.

Stedmon, CA, Amon, RMW, Bauch, D, Bracher, A, Gonçalves-Araujo, R, Hoppmann, M, Krishfield, R, Laney, S, Rabe, B, Reader, H, Granskog, MA. 2021. Insights Into Water Mass Origins in the Central Arctic Ocean From In-Situ Dissolved Organic Matter Fluorescence. *Journal of Geophysical Research: Oceans* **126**(7): e2021JC017407. doi:https://doi.org/10.1029/2021JC017407.

Steele, M, Boyd, T. 1998. Retreat of the cold halocline layer in the Arctic Ocean. *Journal of Geophysical Research: Oceans* **103**(C5): 10419–10435. doi:https://doi.org/10.1029/98JC00580.

Steele, M, Morison, J, Ermold, W, Rigor, I, Ortmeyer, M, Shimada, K. 2004. Circulation of summer Pacific halocline water in the Arctic Ocean. *Journal of Geophysical Research: Oceans* **109**(C2). doi:https://doi.org/10.1029/2003JC002009.

Steele, M, Morley, R, Ermold, W. 2001. PHC3 Updated from: A global ocean hydrography with a high quality Arctic Ocean. *Journal of Climate* **14**(9): 2079–2087. ISSN 1520-0442. doi:https://doi.org/10.1175/1520-0442(2001)

014⟨2079:PAGOHW⟩2.0.CO;2.

Stroeve, J, Serreze, M, Drobot, S, Gearheard, S, Holland, M, Maslanik, J, Meier, W, Scambos, T. 2008. Arctic sea ice extent plummets in 2007. *Eos, Transactions American Geophysical Union* **89**(2): 13–14. doi:https://doi.org/10.1029/2008EO020001.

Takahashi, T, Sutherland, SC, Wanninkhof, R, Sweeney, C, Feely, RA, Chipman, DW, Hales, B, Friederich, G, Chavez, F, Sabine, C, et al. 2009. Climatological mean and decadal change in surface ocean pCO2, and net sea–air CO2 flux over the global oceans. *Deep Sea Research Part II: Topical Studies in Oceanography* **56**(8-10): 554–577. doi:https://doi.org/10.1016/j.dsr2.2008.12.009.

Tanhua, T, Jones, EP, Jeansson, E, Jutterström, S, Smethie Jr, WM, Wallace, DW, Anderson, LG. 2009. Ventilation of the Arctic Ocean: Mean ages and inventories of anthropogenic CO2 and CFC-11. *Journal of Geophysical Research: Oceans* **114**(C1). doi:https://doi.org/10.1029/2008JC004868.

Terhaar, J, Lauerwald, R, Regnier, P, Gruber, N, Bopp, L. 2021. Around one third of current Arctic Ocean primary production sustained by rivers and coastal erosion. *Nature Communications* **12**(1): 169. doi:https://doi.org/10.1038/s41467-020-20470-z.

Timmermans, ML, Toole, JM. 2023. The Arctic Ocean's Beaufort Gyre. *Annual Review of Marine Science* **15**: 223–248. doi:https://doi.org/10.1146/annurev-marine-032122-012034.

Tippenhauer, S, Janout, M, Chouksey, M, Torres-Valdes, S, Fong, A, Wulff, T. 2021. Substantial sub-surface chlorophyll patch sustained by vertical nutrient fluxes in Fram Strait observed with an autonomous underwater vehicle. *Frontiers in Marine Science* **8**: 605225. doi:https://doi.org/10.3389/fmars.2021.605225.

Tippenhauer, S, Vredenborg, M, Heuzé, C, Rabe, B, Ulfsbo, A, Torres-Valdes, S, Budéus, G, Rohardt, G, Wisotzki, A. in prep. Physical oceanography based on lowered CTD data during MOSAiC . *Scientific Data* .

Tippenhauer, S, Vredenborg, M, Heuzé, C, Ulfsbo, A, Rabe, B, Granskog, MA, Allerholt, J, Balmonte, JP, Campbell, RG, Castellani, G, Chamberlain, E, Creamean, J, D'Angelo, A, Dietrich, U, Droste, E, Eggers, L, Fang, YC, Fong, AA, Gardner, J, Graupner, R, Grosse, J, He, H, Hildebrandt, N, Hoppe, CJM, Hoppmann, M, Kanzow, T, Karam, S, Koenig, Z, Kong, B, Kuhlmey, D, Kuznetsov, I, Lan, M, Liu, H, Mallet, M, Mohrholz, V, Muilwijk, M, Müller, O, Olsen, LM, Rember, R, Ren, J, Sakinan, S, Schaffer, J, Schmidt, K, Schuffenhauer, I, Schulz, K, Shoemaker, K, Spahic, S, Sukhikh, N, Svenson, A, Torres-Valdés, S, Torstensson, A, Wischnewski, L, Zhuang, Y. (in review)a. Physical oceanography based on Ocean City CTD during POLARSTERN cruise PS122. PANGAEA. doi:https://doi.pangaea.de/10.1594/PANGAEA.959964.

Tippenhauer, S, Vredenborg, M, Heuzé, C, Ulfsbo, A, Rabe, B, Granskog, MA, Allerholt, J, Balmonte, JP, Campbell, RG, Castellani, G, Chamberlain, E, Creamean, J, D'Angelo, A, Dietrich, U, Droste, E, Eggers, L, Fang, YC, Fong, AA, Gardner, J, Graupner, R, Grosse, J, He, H, Hildebrandt, N, Hoppe, CJM, Hoppmann, M, Kanzow, T, Karam, S, Koenig, Z, Kong, B, Kuhlmey, D, Kuznetsov, I, Lan, M, Liu, H, Mallet, M, Mohrholz, V, Muilwijk, M, Müller, O, Olsen, LM, Rember, R, Ren, J, Sakinan, S, Schaffer, J, Schmidt, K, Schuffenhauer, I, Schulz, K, Shoemaker, K, Spahic, S, Sukhikh, N, Svenson, A, Torres-Valdés, S, Torstensson, A, Wischnewski, L, Zhuang, Y. (in review)b. Physical oceanography based on ship CTD during POLARSTERN cruise PS122. PANGAEA. doi:https://doi.pangaea.de/10.1594/PANGAEA.959963.

Tippenhauer, S, Vredenborg, M, Heuzé, C, Ulfsbo, A, Rabe, B, Granskog, MA, Allerholt, J, Balmonte, JP, Campbell, RG, Castellani, G, Chamberlain, E, Creamean, J, D'Angelo, A, Dietrich, U, Droste, E, Eggers, L, Fang, YC, Fong, AA, Gardner, J, Graupner, R, Grosse, J, He, H, Hildebrandt, N, Hoppe, CJM, Hoppmann, M, Kanzow, T, Karam, S, Koenig, Z, Kong, B, Kuhlmey, D, Kuznetsov, I, Lan, M, Liu, H, Mallet, M, Mohrholz, V, Muilwijk, M, Müller, O, Olsen, LM, Rember, R, Ren, J, Sakinan, S, Schaffer, J, Schmidt, K, Schuffenhauer, I, Schulz, K, Shoemaker, K, Spahic, S, Sukhikh, N, Svenson, A, Torres-Valdés, S, Torstensson, A, Wischnewski, L, Zhuang, Y. (in review)c. Physical oceanography water bottle samples based on ship CTD during POLARSTERN cruise PS122. PANGAEA. doi:https://doi.pangaea.de/10.1594/PANGAEA.959965.

Tippenhauer, S, Vredenborg, M, Heuzé, C, Ulfsbo, A, Rabe, B, Granskog, MA, Allerholt, J, Balmonte, JP, Campbell, RG, Castellani, G, Chamberlain, E, Creamean, J, D'Angelo, A, Dietrich, U, Droste, E, Eggers, L, Fang, YC, Fong, AA, Gardner, J, Graupner, R, Grosse, J, He, H, Hildebrandt, N, Hoppe, CJM, Hoppmann, M, Kanzow, T, Karam, S, Koenig, Z, Kong, B, Kuhlmey, D, Kuznetsov, I, Lan, M, Liu, H, Mallet, M, Mohrholz, V, Muilwijk, M, Müller, O, Olsen, LM, Rember, R, Ren, J, Sakinan, S, Schaffer, J, Schmidt, K, Schuffenhauer, I, Schulz, K, Shoemaker, K, Spahic, S, Sukhikh, N, Svenson, A, Torres-Valdés, S, Torstensson, A, Wischnewski, L, Zhuang, Y. (in review)d. Physical oceanography water bottle samples based on Ocean City CTD during POLARSTERN cruise PS122. PANGAEA. doi: https://doi.pangaea.de/10.1594/PANGAEA.959966.

Toole, JM, Krishfield, R. 2016. Woods Hole Oceanographic Institution Ice-Tethered Profiler Program. Ice-Tethered Profiler observations: Vertical profiles of temperature, salinity, oxygen, and ocean velocity from an Ice-Tethered Profiler buoy system. [ITP94, ITP111, Accessed March 13. 2023]. NOAA National Centers for Environmental Information. doi:https://doi.org/10.7289/v5mw2f7x.

Toole, JM, Krishfield, RA, Timmermans, ML, Proshutinsky, A. 2011. The ice-tethered profiler: Argo of the Arctic. *Oceanography* **24**(3): 126–135. doi: https://doi.org/10.5670/oceanog.2011.64.

Toole, JM, Timmermans, ML, Perovich, DK, Krishfield, RA, Proshutinsky, A, Richter-Menge, JA. 2010. Influences of the ocean surface mixed layer and thermohaline stratification on Arctic Sea ice in the central Canada Basin. *Journal of Geophysical Research: Oceans* **115**(C10). doi:https://doi.org/10.1029/2009JC005660.

Torres-Valdés, S, Tsubouchi, T, Bacon, S, Naveira-Garabato, AC, Sanders, R, McLaughlin, FA, Petrie, B, Kattner, G, Azetsu-Scott, K, Whitledge, TE. 2013. Export of nutrients from the Arctic Ocean. *Journal of Geophysical Research: Oceans* **118**(4): 1625–1644. doi:https://doi.org/10.1002/jgrc.20063.

von Appen, WJ, Schauer, U, Somavilla, R, Bauerfeind, E, Beszczynska-Möller, A. 2015. Exchange of warming deep waters across Fram Strait. *Deep Sea Research Part I: Oceanographic Research Papers* **103**: 86–100. doi:https://doi.org/10.1016/j.dsr.2015.06.003.

Wang, Q, Shu, Q, Bozec, A, Chassignet, EP, Fogli, PG, Fox-Kemper, B, Hogg, AM, Iovino, D, Kiss, AE, Koldunov, N, Le Sommer, J, Li, Y, Lin, P, Liu, H, Polyakov, I, Scholz, P, Sidorenko, D, Wang, S, Xu, X. 2023. Impact of high resolution on Arctic Ocean simulations in Ocean Model Intercomparison Project phase 2 (OMIP-2). *Geoscientific Model Development Discussions* **2023**: 1–46. doi:https://doi.org/10.5194/gmd-2023-123.

Webster, MA, Holland, M, Wright, NC, Hendricks, S, Hutter, N, Itkin, P, Light, B, Linhardt, F, Perovich, DK, Raphael, IA, et al. 2022. Spatiotemporal evolution of melt ponds on Arctic sea ice: MOSAiC observations and model results. *Elementa Science of the Anthropocene* **10**(1): 000072. doi:https://doi.org/10.1525/elementa.2021.000072.

Zhao, M, Timmermans, ML, Cole, S, Krishfield, R, Proshutinsky, A, Toole, J. 2014. Characterizing the eddy field in the Arctic Ocean halocline. *Journal of Geophysical Research: Oceans* **119**(12): 8800–8817. doi:https://doi.org/10.

1002/2014JC010488.

Zweng, M, Reagan, J, Seidov, D, Boyer, T, Locarnini, R, Garcia, H, Mishonov, A, Baranova, O, Weathers, K, Paver, C, Smolyar, I. 2018. *World Ocean Atlas 2018, Volume 2: Salinity*. A. Mishonov Technical Ed.; NOAA Atlas NESDIS 82.